Patient-specific parameter estimation in single-ventricle lumped circulation models under uncertainty

Daniele E. Schiavazzi[1,*,†], **Alessia Baretta**[2], **Giancarlo Pennati**[2], **Tain-Yen Hsia**[3], and **Alison L. Marsden**[4]

[1]Department of Pediatrics, Stanford University, Stanford, CA, USA

[2]Department of Chemistry, Materials and Chemical Engineering, Politecnico di Milano, Milano, Italy

[3]Great Ormond Street Hospital for Children and UCL Institute of Cardiovascular Science, London, UK

[4]Department of Pediatrics, Bioengineering and ICME, Stanford University, Stanford, CA, USA

Summary

Computational models of cardiovascular physiology can inform clinical decision-making, providing a physically consistent framework to assess vascular pressures and flow distributions, and aiding in treatment planning. In particular, lumped parameter network (LPN) models that make an analogy to electrical circuits offer a fast and surprisingly realistic method to reproduce the circulatory physiology. The complexity of LPN models can vary significantly to account, for example, for cardiac and valve function, respiration, autoregulation, and time-dependent hemodynamics. More complex models provide insight into detailed physiological mechanisms, but their utility is maximized if one can quickly identify patient specific parameters. The clinical utility of LPN models with many parameters will be greatly enhanced by automated parameter identification, particularly if parameter tuning can match non-invasively obtained clinical data. We present a framework for automated tuning of 0D lumped model parameters to match clinical data. We demonstrate the utility of this framework through application to single ventricle pediatric patients with Norwood physiology. Through a combination of local identifiability, Bayesian estimation and maximum a posteriori simplex optimization, we show the ability to automatically determine physiologically consistent point estimates of the parameters and to quantify uncertainty induced by errors and assumptions in the collected clinical data. We show that multi-level estimation, that is, updating the parameter prior information through sub-model analysis, can lead to a significant reduction in the parameter marginal posterior variance. We first consider virtual patient conditions, with clinical targets generated through model solutions, and second application to a cohort of four single-ventricle patients with Norwood physiology.

[*]Correspondence to: Daniele E. Schiavazzi, Department of Pediatrics, Stanford University, Stanford, CA, USA.
[†]danschi@stanford.edu

Keywords

Bayesian estimation; lumped circulation models; patient-specific data assimilation; uncertainty analysis of simulated physiology; single-ventricle surgery; Norwood procedure

1. Introduction

Recent developments in medical imaging, computational mechanics, and uncertainty analysis of computer models are now enabling non-invasive assessment of hemodynamics through patient specific simulations. Use of this approach is particularly promising when clinical data collection is limited due to patient risk or ethical considerations.

Use of computer models to simulate the human circulation dates back to the late 1960s, where analog computer surrogates of the human cardiovascular system were formulated to investigate mechanisms of venous return and physiologic response during unusual acceleration conditions [1]. These models share the same governing equations with electrical circuits in which flow is analogous to current and pressure drop is analogous to voltage. Improved lumped modeling for the human ventricle was proposed in the 1980s [2], followed by applications to closed-loop cardiovascular systems [3].

Our focus in this paper is on physiologies characterized by the presence of a single functional ventricle. These are caused by severe forms of congenital heart disease, typically treated by surgical transition to the Fontan circulation, where a series arrangement is restored between the systemic and pulmonary blood flow [4]. Because of the high PVR typically observed in the early stages of life and to allow the patient to gradually adapt to the new circulation paradigm, palliation of single-ventricle is typically preformed in stages. Three stages are usually implemented: Norwood procedure (stage I [5]), superior cavopulmonary connection (SCPC stage II, either bi-directional Glenn or hemi-Fontan surgeries) and Fontan completion (stage III). We are particularly interested in the first stage of palliation, associated with the highest reported mortality [6]. Applications of lumped parameter network (LPN) models to study this specific physiology are reported in [7] and in [8]. Recent review articles also discuss modeling approaches to study the Fontan circulation [9] as well as physiologies characterized by an implanted systemic-to-pulmonary shunt [10].

Complex LPN models may include detailed sub-models of organs, effect of respiration and autoregulatory mechanisms (see, e.g., [11]) and have been shown to accurately reproduce normal and pathologic physiology. However, prognostic use of these models is often hindered by the difficulty of estimating patient specific parameter values. In other words, complex models are likely to contain unidentifiable parameter combinations due to model non-linearity, and possible inconsistencies in the clinical measurements. Thus, manual tuning is often adopted in practice but suffers from non-repeatability, high user-time requirements, and failure to account for clinical data uncertainty. Automated tuning is, in our opinion, critical to the use of lumped circulation models for patient specific simulations. Moreover, these models are cheap to solve on a modern computer and therefore well suited to optimization and uncertainty quantification for which multiple model solutions are needed.

Several approaches to automatic tuning have been proposed in the literature. Some have included automatic parameter estimation of three-element Windkessel open-loop boundary conditions [12], or iterative parameter identification of sub-compartments, thus reducing the number of parameters identified simultaneously [13, 14]. Others have proposed optimization, sensitivity analysis, recursive least squares, auto-regressive models, and Kalman filtering [15–24].

This study focuses on pre-operative model tuning for surgical planning in single-ventricle palliation surgery. In this context, the ability to accurately simulate the physiological transition between two successive stages is greatly affected by both the fidelity in representing local hemodynamics and the availability of an accurate representation of the peripheral and cardiac circulations in the patient. Capturing both local and circulatory pre-operative hemodynamics ensures that the post-operative physiology is well captured after the change in circulatory layout (represeting the immediate postoperative patient conditions). This can only be achieved when the heart model parameters are reliably identified, and when the correct distribution of circulatory resistances and compliances (typically associated with significant inter-patient variability) are well captured. We therefore develop an effective pre-operative model identification strategy (‘a necessary preliminary step’, as discussed in [25, 26]) for over-parameterized LPN models and show how clinical data uncertainty affects this process. The proposed LPN formulation includes a detailed non linear description of the cardiac contraction mechanism to realistically model patients with severe heart pathologies and capture post-operative changes.

While prior approaches have focused either on cycle-averaged targets or on the availability of time-dependent patient data (rarely available in practice), the proposed approach offers more flexibility to account for multiple time statistics (e.g., average, maximum and minimum values of target quantities) and peaks in the pressure/flow rate curves. Also, prior approaches have mostly been applied to LPN layouts with few elements or have made use of *a priori* information to significantly reduce the number of parameters. Finally, although many studies in the literature (see, e.g., [15, 17, 20–24]) employ a Bayesian representation of the unknown parameters through a vector of random variables, they often aim primarily to determine optimal parameter estimates, without deriving associated confidence metrics.

We present an application of Bayesian estimation with adaptive MCMC as a means to generate samples from the joint distribution of the 0D model parameters. This is complemented by a preliminary analysis of the Fisher Information matrix (FIM) rank and eigenvectors, to determine unimportant parameter combinations. Prior knowledge is specified either in the form of admissible ranges (from experience, expert judgment) or through a multi-level approach, where priors are updated from analysis of circulation sub-models. Maximum a posteriori (MAP) parameter estimates are finally computed using simplex optimization.

The LPN models used in this study are first derived in Section 2 with details reported in the Appendix. This is followed, in Section 3, by a discussion of the clinical data collection and the selection of target quantities and parameter ranges for patient-specific simulations. In Section 4, we discuss the formulation of the statistical estimation problem and introduce the

numerical algorithms used for identifiability analysis, multi-level adaptive MCMC and MAP optimization. A computational framework supporting both single-level and multi-level estimation for LPN model parameters is presented in Section 4.5. Results are presented in Section 5, first for a simplified peripheral circulation model (Section 2.1), and then for a complete model of the Norwood circulation subject to *virtual patient* (Section 5.2) and *patient specific* conditions (Section 5.3). Finally, conclusions and future work are discussed in Section 6. The acronyms used throughout the paper are listed in Table I.

2. Lumped Parameter Models

In this section, we describe the three LPN models that will be used for our numerical investigations in Section 5. These are: *i)* a RCRCR representation of the peripheral circulation; *ii)* a submodel of the heart with prescribed venous and aortic flows, and *iii)* a complete closed-loop LPN circulation model, including the heart, pulmonary and systemic circulations, and systemic-to-pulmonary shunt.

2.1. RCRCR model

RCRCR blocks are typically used (in combination with inductance elements), to mimic the peripheral circulation and organ blocks (e.g., lungs, liver, intestine, etc.), with the three resistance values, R_1, R_2, and R_3, typically used to represent the arterial, capillary and venous resistances (see, e.g., [25]), and the capacitances, C_1 and C_2, associated with the arterial and venous compliances, respectively (Figure 1a). Pressure is defined at four locations, P_0, P_1, P_2, P_3, while flow rates Q_1, Q_2, Q_3 are defined at the respective resistors R_1, R_2, R_3. The inlet and outlet flow rates Q_1 and Q_3, assumed periodic, are prescribed in terms of a truncated Fourier coefficient expansion, see appendix A.

The system has 7 parameters: the total resistance $R_{tot} = R_1 + R_2 + R_3$, $\tau = R_{tot}\, C_{tot}$, where $C_{tot} = C_1 + C_2$, the compliance ratio ($C1/C2$), the resistance ratios (R_1/R_2), (R_3/R_2) and the initial conditions for P_1 and P_2. ODE models for RCRCR circuits are obtained by combining basic formulations from simpler RC components, that is,

$$Q = \frac{P_{\mathrm{up}} - P_{\mathrm{dw}}}{R}, \quad \frac{dP_{\mathrm{dw}}}{\mathrm{dt}} = \frac{Q_{\mathrm{up}} - Q_{\mathrm{dw}}}{C}, \quad (1)$$

where P_{up}, P_{dw}, Q_{up}, and Q_{dw} denote the upstream and downstream pressures and flow rates, respectively.

2.2. Heart sub-model

The heart model illustrated in Figure 1(b) consists of five main components: single atrium, atrioventricular (AV) valve, single ventricle, aortic valve and aorta (AO), and is characterized by 20 parameters (Table II), including resistance and compliance elements, parameters characterizing atrial and ventricular contractility, and nonlinear diodes for the AV and aortic valves. It includes four state variables, the atrial and ventricular volumes V_{sv} and V_{sa}, the aortic pressure P_{ao} and the AV flowrate Q_{av}. The aortic and venous flow rates are prescribed as boundary conditions using the Fourier coefficients reported in the Appendix.

The interested reader is referred to the literature on the subject (see, e.g., [2, 3, 27]) for a in-depth discussion on this lumped parameter formulation.

2.3. Norwood circulation models

A schematic representation of a complete circulation model used to study stage I single-ventricle physiology is illustrated in Figure 1(c). It includes three main compartments: the heart, systemic, and pulmonary circulations. The heart model is the same as described in the previous section, while circulatory blocks in the upper/lower body and the lungs are modeled using RLCRCR circuits. The systemic-to-pulmonary shunt combines linear and nonlinear resistive components, accounting for both major and minor (e.g., shunt-pulmonary anastomosis) pressure losses [28]. Both resistive terms are parameterized as functions of the shunt equivalent diameter D_{sh} (see detailed formulation in the Appendix). The effects of coronary circulation, gravity, and respiration are neglected [28].

For the arterial blocks (subscript '1' in Figure 1(c)), which include inertance, Equation (1) is re-formulated as

$$\frac{dQ}{\mathrm{dt}} = \frac{P_{\mathrm{up}} - P_{\mathrm{dw}} - R \cdot Q}{L}. \quad (2)$$

The sum of arterial, capillary bed and venous resistances $R_{tot} = R_{art} + R_{bed} + R_{ven} = R_1 + R_2 + R_3$ is set equal to the total systemic and pulmonary vascular resistances (SVR and PVR, which can be clinically measured, as reported in Section 3.1), while total compliance for upper/lower body and lungs is related to the associated vascular resistance as $C_{tot} = \tau/R_{tot}$. Ranges for τ are determined from the literature [29–31]. Resistances and compliances in the peripheral circulation blocks are determined through the ratios (R_1/R_2, R_3/R_2, C_1/C_2) with ranges from literature data representing separate contributions of arterial, capillary bed, and venous circulation [30, 31].

The resulting system of ODEs is solved numerically using a 4th order Runge-Kutta scheme with constant time step size (4.0×10^{-4} s in the present study) for all models. The full list of equations used can be found in the Appendix.

3. Clinical Data Collection and Target Selection

Following the parameter definitions and ODE model formulation, we now identify the target clinical quantities that should be matched by model outputs following an optimal parameter selection. With reference to these targets, the results in Section 5 will refer to *virtual* or *patient specific* conditions. In the former case model outputs resulting from known input parameter sets will be used, while in the latter case, clinically collected targets will be directly employed. Finally, we discuss an *a priori* selection for the ranges of model parameters subject to identification.

3.1. Clinical data collection

Four patients were enrolled in the study at medical centers in Europe and the US, after institutional review board approval and obtaining informed consent (Table III). These centers included the Medical University of South Carolina (patient MUSC7), Great Ormond Street Hospital in London (patient GOSH22) and the University of Michigan Medical Center (patients UM5 and UM10). For each patient, clinical data were collected, including catheterization-derived pressure tracings, MRI flow tracings and echo-Doppler velocity tracings. Clinical measurements were obtained prior to the stage II procedure, from a few hours up to a few weeks prior to the date of surgery. Pre-operative echocardiograms were performed under sedation following routine clinical protocols, while MRI was performed under general anesthesia for each patient. Cardiac catheterization for pre-operative testing was performed under conscious sedation, using routine clinical protocols. Flow measurements were obtained using an ECG-gated, free-breathing, cine-phase contrast velocity-encoded pulse sequence, and commercially available cardiac analysis software.

Volumetric blood flow rates were acquired through MRI at the ascending AO, inferior vena cava (IVC) and superior vena cava (SVC), pulmonary veins (PV) and pulmonary arteries (PA). Velocities in the AO, inferior vena cava, superior vena cava, atrio-ventricular valve and Blalock-Thomas-Taussig (BT) shunt were also collected using echo-Doppler and consistency between MRI and echo-Doppler measurements was assessed based on reasonable differences in the patient's heart rate. Blood pressure was collected at the AO, atrium, ventricle and only indirectly in the PA using wedge pressures recorded in the pulmonary veins (PVW). Figure 2 summarizes locations in the circulation layout, where MRI, echo-Doppler or catheter data were collected. In this figure, two measurement locations are shown for the pulmonary venous flow to indicate that at least one measure was present for each side (flow returning from the left or right lung). First, the consistency among collected flow data was verified (i.e., the cardiac output, calculated as cycle-averaged flow Q_{ao} has to be equal to Q_{ven} calculated as the sum of all the cycle-averaged venous flow). In case of small differences (typically observed in clinical measurements) the flow data were properly scaled to respect conservation of mass. Two possible approaches were adopted in this context, depending on a reliability assessment of measured MR flow from the clinicians in our research group: either the most reliable between the two flows (Q_{ao} or Q_{ven}) was kept unchanged, correcting the other one, or both flows were corrected, considering their average as the most reliable estimate. Then, patient-specific pulmonary vascular resistances (PVR, SVR) were derived using the ratio of the pressure drop across the compartment of interest to the flow passing through it, that is,:

$$\mathrm{PVR}=\frac{P_{\mathrm{pa}}-P_{\mathrm{sa}}}{Q_{\mathrm{RPV}}+Q_{\mathrm{LPV}}},\quad \mathrm{SVR}=\frac{P_{\mathrm{ao}}-P_{\mathrm{sa}}}{Q_{\mathrm{SVC}}-Q_{\mathrm{IVC}}}, \tag{3}$$

where P_{pa}, P_{sa}, and P_{ao} represent the cycle-averaged values of main pulmonary artery (estimated using PVW), atrial and ascending AO pressures, Q_{RPV}, Q_{LPV}, Q_{SVC}, Q_{IVC} denote the cycle-averages of right and left pulmonary and upper and lower body systemic flows, respectively. Note how Q_{RPV} and Q_{LPV} in (3) correspond to the sum of the flows

measured in the left or the right PV, respectively (one or two veins, depending on the selected patient).

SVR and PVR for the four patients, AV valve area segmented from clinical image data and heart rates are repoted in Table III. Note that the heart rate is a known parameter and it is not subject to estimation.

3.2. Clinical target selection

Atrial, ventricular, and aortic pressures are included as clinical targets both in the heart sub-models (Section 2.2) and full Norwood circulation models (Section 2.3). Mean and maximum aortic pressures $P_{ao,av}$, $P_{ao,max}$ are included as targets for the heart sub-model, while the minimum values $P_{ao,min}$ are also considered in the Norwood model, to capture physiologically realistic pulsatility.

The minimal ventricular pressure $P_{sv,min}$ is not included as a target quantity due to its close relationship with the atrial pressure $P_{sa,av}$. The end diastolic pressure (EDP) is in fact related to $P_{sv,min}$ through the passive ventricular curve, typically having a small slope in the pressure-volume plane. Thus, values of $P_{sa,av}$ should be similar to EDP and, in turn, to $P_{sv,min}$. Proper identification of the atrial parameters is therefore expected to produce a reasonable estimate of the minimum ventricular pressure.

In the ventricle, the cardiac output CO is prescribed either directly (Norwood model) or through the time history of the aortic flow rate (heart sub-model). $V_{sv,min}$ can therefore be automatically determined as $V_{sv,min} = V_{sv,max} - CO \cdot HR$. The prescription of the minimum ventricular volume (although being indirectly imposed) is expected to help in the proper identification of the unstressed volume of the single ventricle $V_{sv,0}$. Other target quantities included the average regurgitation flow rate (patient UM10 only), the Q_p/Q_s ratio and the average minimum and maximum pulmonary artery pressures $P_{pa,av}$, $P_{pa,min}$, $P_{pa,max}$.

Moreover, we wanted the Norwood model to generate venous flow rate time histories matching the clinical measurements and consistent with those prescribed to the heart sub-model. As venous flow is characterized by a bi-phasic waveform (for single ventricle patients with aorto-pulmonary shunts see, e.g., [32]), we used the systolic peak (S), the diastolic peak (D) and the two minima between these peaks (M and A, respectively) to quantify the agreement between clinical and simulated venous flow rates.

Finally, standard deviations of clinical measurements were estimated using 5% of their expected values (compatible with observations in intensive care units, see e.g., [13]), and amplified with weights inversely proportional to their clinical importance. For example, a weight of 1/2 was assigned to both $P_{ao,av}$ and CO, which we considered the most critical targets to match. A unit weight is applied to all other targets, except SMDA locations in venous curves. In this case, a weight of eight was applied to the systemic SMDA targets and 12 to the PV. With eight targets for venous flow rates at SMDA locations, these higher weights ensured that the posterior was not excessively dependent on the agreement for these quantities, for which the confidence in the clinical tracings is relatively low. Higher weights were assigned to the pulmonary rather than the systemic circulation blocks, as they seem to

consistently generate better registration results. This is likely due to the higher complexity of estimating the pulmonary circulation parameters, as they are in series with the non linear shunt compartment.

A complete list of the selected clinical targets is reported in Table IV. Echo-Doppler tracings (namely AV valve velocity and shunt velocity) were not used as targets for identification, as they were often recorded under HR conditions quite different from the HR measured during the MR aquisition.

3.3. Parameter ranges

Parameter ranges (Table V) were determined from literature data and previous experience with manual tuning. The ratios between atrial and ventricular activation times and heart cycle duration were constrained based on literature data [28]. Ranges of systemic and pulmonary compliances (i.e., $C_{tot} = C_1 + C_2$) were obtained by assuming the quantity $\tau = C_{tot} R_{tot}$ to vary in the interval [0.5, 3.0] [29–31]. Use of ratios for activation times, resistances, and compliances in the pulmonary and systemic circulations, allows us to reduce the overall number of parameters (e.g., by prescribing PVR and SVR measurements), and often leads to a reduced variability in the associated ranges (e.g., use of the time constant τ instead of the total compliance C_{tot}).

4. Methodology

4.1. Statistical model

We consider a set of d parameters $\mathbf{y} = [y_1, y_2, \ldots, y_d] \in \Omega \subset \mathbb{R}^d$ statistically characterized through their joint probability distribution $\rho(y_1, y_2, \ldots, y_d)$ and denote $\mathbf{y}^k$ as the generic k-th realization. The circulation model $\mathbf{G} : \mathbb{R}^d \rightarrow \mathbb{R}^m$ establishes a typically non-linear relationship between $\mathbf{y}^k$ and the realization $\mathbf{o}^k$ of the outputs $\mathbf{o} = [o_1, o_2, \ldots, o_m] \in \mathbb{R}^m$, or, in other words $\mathbf{o} = \mathbf{G}(\mathbf{y})$. Direct or indirect measurements for quantities of clinical relevance are expressed through the random variables $\mathbf{d} = [d_1, d_2, \ldots, d_m] \subset \mathbb{R}^m$ with joint distribution $\rho(d_1, d_2, \ldots, d_m)$ assumed Gaussian with average equal to the model response $\mathbf{G}(\mathbf{y})$ and diagonal covariance $\mathbf{C}_d$, consistent with a statistical model of the form

$$\mathbf{d} = \mathbf{G}(\mathbf{y}) + \epsilon. \quad (4)$$

In Equation (4) the error term $\epsilon \sim N(0, \mathbf{C}_d)$ combines errors introduced by both experimental data and model formulation. An unknown, full covariance $\mathbf{C}_d$ could be estimated as suggested in [33, 34] by assimilating differential circulation models to *multiresponse* systems. These are characterized by multiple sets of possibly correlated observations (e.g., pressures and flow rates at various locations). In our case, $\mathbf{C}_d$ is not full but typically block diagonal, due to the different physiological conditions commonly observed during clinical measurements of blood pressures (i.e., catheter measurements on a sedated patient) and flow rates (i.e., acquired through non-invasive MRI or echoDoppler). Finally, the lack of data on the correlation between pressure or between flow rate

measurements suggests the adoption of a diagonal covariance. As a result of these assumptions, the likelihood function assumes the form

$$P(\mathbf{d}|\mathbf{y})\frac{1}{\sqrt{(2\pi)^m\prod_{i=1}^m\omega_i\sigma_i^2}}\exp\left(-\frac{1}{2}\sum_{i=1}^m\frac{[d_i-G_i(y)]^2}{w_i\sigma_i^2}\right). \quad (5)$$

where we added the weights w_i for each clinical target, as discussed in Section 3.2. The parameter posterior is finally formulated through Bayesian conjunction

$$P(\mathbf{y}|\mathbf{d}) \propto P(\mathbf{d}|\mathbf{y})P(\mathbf{y}). \quad (6)$$

In our study, we use uniform priors if no previous information is available for a specific parameter, while we use independent Gaussians for parameters whose first and second moments are available from previous analysis (i.e., multi-level estimation discussed in Section 5).

4.2. Local and global parameter identifiability

Before proceeding further, it is important to understand if and under what circumstances it is possible to estimate the parameters of a given system from the available data, that is, if the system is *identifiable*. A review of several methodologies on identifiability is provided in [35] in the context of nonlinear ODE models of viral dynamics. Two methodologies are used in this work to detect unimportant parameters or non identifiable combinations of parameters.

First, we investigate the FIM rank as a *local* measure of identifiability, that is, the ability to learn parameters in a neighborhood of a specific realization under varying availability of measured data [36]. As a direct result of assuming the likelihood in Equation (5), we have:

$$\mathscr{I}(\mathbf{y})=\left[\frac{\partial\mathbf{G}(\mathbf{y})}{\partial\mathbf{y}}\right]^T\mathbf{C}_d^{-1}\left[\frac{\partial\mathbf{G}(\mathbf{y})}{\partial\mathbf{y}}\right]. \quad (7)$$

Note that Equation (7) is easily obtained by combining the matrix $\partial\mathbf{G}(\mathbf{y})/\partial\mathbf{y}\in\mathbb{R}^{d\times m}$ of local derivatives (e.g., computed using a finite difference approximation) with the diagonal matrix $\mathbf{C}_d^{-1}$ obtained from the assumed precisions (inverse variances) associated with the available targets. As discussed in [36] the rank of $\mathscr{I}(\mathbf{y})$ reveals the presence of non-identifiable combinations of parameters, and an analysis of the eigenvectors associated with the zero eigenvalues (the so-called *null eigenvectors*) can be useful to identify such combinations.

Second, we propose systematic MAP estimation. The FIM approach discussed above provides information on the identifiability at specific locations in parameter space, that is,

those selected to calculate the matrix $\partial\mathbf{G}(\mathbf{y})/\partial\mathbf{y}$. To better understand the degree of convexity of the posterior distribution, we select a realization $\mathbf{y}^*$ in parameter space and evaluate the corresponding virtual targets $\mathbf{o}^* = \mathbf{G}(\mathbf{y}^*)$. We then try to recover the parameters $\mathbf{y}^*$ from $\mathbf{o}^*$ by performing MAP estimation (i.e., determining the maximum of the posterior distribution using optimization) starting from random locations in parameter space within a prior admissible range. We denote the MAP parameter estimate determined through optimization as $\hat{\mathbf{y}}$. Finally, we report the results in a graph, where the maximum posterior value resulting from optimization is plotted on the abscissa, while the ℓ_2 distance between $\hat{\mathbf{y}}$ and $\mathbf{y}^*$, that is, $d_y = \sqrt{\frac{1}{d}\sum_{i=1}^{d}[(y_i^* - \hat{y}_i)/(y_{i,u} - y_{i,l})]^2}$, is plotted on the ordinate and $y_{i,u}$, $y_{i,l}$ are the upper and lower bounds for parameter y_i.

We use these strategies, together with posterior probability profiling to reveal features in the objective function (or posterior distribution) that are otherwise difficult to understand in several dimensions.

4.3. Differential Evolution adaptive Metropolis estimation

As discussed in Section 5, issues of non-identifiability in over-parametrized models typically result in non-convex posterior distributions with an abundance of local minima/maxima. This prevents optimization methods from efficiently finding the parameter set associated with a global posterior maximum. Moreover, we are also interested in characterizing the variability in our estimate of the parameters.

This justifies our choice of performing Bayesian parameter identification, using MCMC [37, 38] to iteratively sample from the posterior $P(\mathbf{y}|\mathbf{d})$. It is well known that specification of prior knowledge can substantially improve parameter learning in a Bayesian framework [39]. A Bayesian approach also provides ways to detect unidentifiable parameter combinations. For example, marginal posteriors that resemble uniform distributions may indicate low sensitivity or unimportant parameters. Non identifiable combinations involving three or more parameters, may be also detected from a heat map of the correlation matrix (see, e.g., [40]).

Many MCMC algorithms have been proposed in the literature. Because of the non-linearity of **G**, the likelihood in Equation (5) is not generally normally distributed, and classical random walk Metropolis may exhibit slow convergence in such cases. Numerous approaches are discussed in the literature (see, e.g., [41–47]) to automatically adapt the scale and orientation of the trial distribution to achieve faster convergence while still satisfying *detailed balance* (see, e.g., [48, 49]). Differential evolution adaptive Metropolis (DREAM) [50] combines differential evolution [51] and self adaptive randomized subspace sampling from $N < d$ multiple Markov chains $\{\mathbf{y}_i^k, i = 1, \ldots, N\}$, to adapt the scaling and orientation of the trial distribution without explicitly updating its covariance. It also shows a substantial improvement with respect to other adaptive MCMC schemes when sampling from heavy tailed or multi-modal posteriors, and we have adapted this approach for the present problem as described below.

Convergence is assessed using the Gelman-Rubin (GR) diagnostic [52]. Extensions of DREAM are discussed, for example, in [53] where parallel implementation in combination with a multiple-try-Metropolis strategy were used to sample from hydrologic models with up to 241 random parameters.

It is worth noting that DREAM performs a random exploration of Ω, asymptotically generating samples from a distribution proportional to $\rho(y_1, y_2, \ldots, y_d)$. This exploration can be used to improve the robustness of an optimization-based MAP estimate of the parameters, with clear similarities to stochastic optimization algorithms such as simulated annealing [54]. In practice, we start from the parameter set that maximizes the posterior during DREAM and employ gradient-free hillclimb optimization (i.e., Nelder-Mead (NM) simplicial optimization [55, 56]) to further refine our MAP estimate. This reduces the chance that our optimal parameter set will be trapped in a local posterior maximum.

4.4. Multi-level Bayesian estimation

Parameter estimation under virtual patient conditions using the Norwood model was first performed using uninformative parameter priors. Both identifiability and Bayesian estimation results showed that the heart sub-model is the main source of non-identifiability, with a regular FIM typically resulting from fixing the heart parameters.

We therefore take advantage of both the compartmental nature of our circulation models and the underlying Bayesian framework, and propose a multi-level estimation strategy, where parameter posteriors determined through the heart sub-model provide informative priors for estimation of parameters in the full Norwood model. Accordingly, we partition the parameter set $\mathbf{y}$ into heart model parameters $\mathbf{y}_h \in \mathbb{R}^{dh}$ and full model parameters $\mathbf{y}_f \in \mathbb{R}^{df}$, where clearly $d_h + d_f = d$. Registration of heart sub-model parameters provides the posterior $P_h(\mathbf{y}_h|\mathbf{d})$ that is used to *update* the full circulation posterior as follows:

$$P(\mathbf{y}|\mathbf{d}) \propto P(\mathbf{d}|\mathbf{y}) P_f(\mathbf{y}_f) P_h(\mathbf{y}_h|d), \quad (8)$$

where $P_f(\mathbf{y}_f)$ identifies the prior knowledge for the parameters $\mathbf{y}_f$. We note that this two-level Bayesian update can be generalized to multiple levels by increasing the number of sub-models. Iterative tuning of separate compartments is, for example, applied in [13] and seems to offer an interesting regularization mechanism, which could be explored further in future work.

4.5. Computational framework

A schematic of the computational framework developed for this study is illustrated in Figure 3. This is designed to automatically run DREAM on multiple models (e.g., the heart sub-model and full Norwood model), followed by NM optimization. Optionally, multi-level estimation can be performed by first running the heart sub-model and then exchanging prior information before running the full Norwood circulation model.

Single-level parameter estimation is performed following path 2–4, that is, without taking advantage of the underlying nested model arrangement. Multi-level estimation is carried out following path 1–5–4. Identifiability of the heart model is first assessed, followed by estimation of the heart sub-model parameters through adaptive MCMC. Estimation of the complete set of circulation parameters using refined heart parameter priors is finally carried out.

5. Results

5.1. RCRCR Model

We first explore the application of the above tools to a reduced representative RCRCR model shown in Figure 1(a). A parameter set is selected for identifiability analysis as (R_{tot}, τ, C_1/C_2, R_1/R_2, R_3/R_2, $P_{1,i}$, $P_{2,i}$) = $\mathbf{y}^*$ = (3.07, 0.56, 0.2, 0.2, 0.2, 5.0, 5.0), and a diagonal covariance $\mathbf{C}_d$ assembled using standard deviations equal to 5% of the associated model solutions. The total number of parameters for this model is 7 (including initial conditions on P_1 and P_2) with 21 available targets (minimum, average and maximum pressure and flow rate at all locations). Analysis of identifiability and parameter estimation are performed for this model under 4 scenarios, with differences in the number of parameters to identify and available measurements to be matched:

- **Scenario 1**: all 7 parameters need to be determined from all targets.
- **Scenario 2**: 5 parameters need to be determined from 5 targets.
- **Scenario 3**: 5 parameters need to be determined from 3 targets.
- **Scenario 4**: 3 parameters need to be determined from 5 targets.

Parameters and targets for each scenario are provided in Table VI. Note that scenario 1 is characterized by a complete knowledge of the available measurements and by including the initial conditions as parameters. The other 3 scenarios were instead selected to test identifiability in situations characterized by equal number of parameters and measurements (scenario 2), more parameters than measurements (scenario 3), more measurements than parameters but without including initial conditions (scenario 4).

5.1.1. Local Identifiability—Figure 4 shows the matrix $\partial\mathbf{G}(\mathbf{y})/\partial\mathbf{y}$ of local sensitivities. The following features are apparent: input and output flow rates Q_1 and Q_3 are prescribed quantities and result in zero sensitivities (not shown); the total resistance R_{tot} does not influence the flowrate Q_2, as expected; derivatives of $\mathbf{G}(\mathbf{y})$ with respect to the initial pressure conditions are equal for all output pressures and zero for the flow rates. From the above sensitivities, rank and eigenvectors of $\mathcal{A}(\mathbf{y})$ are computed as in (7), with the following results obtained for the four scenarios:

Scenario 1: The eigenvalues are (0.000, 2.052, 441.938, 4110.692, 8593.620, 12941.682, 189749, 442). The FIM is therefore rank deficient with null eigenvector equal to (0.0, 0.0, 0.0, 0.0, 0.0, 0.9806, −0.1962). This is consistent with the observed constant sensitivities, meaning that any opposite change in the pressure initial conditions with relative magnitude proportional to the null eigenvector does not alter the output pressures and flow rates in the

model. This is an interesting case, as non-identifiable combinations of parameters are observed in a situation characterized by an abundance of available measurements.

Scenario 2: Eigenvalues are obtained in the range [0.413, 101.384 × 10^3]. No eigenvalue is zero in this case, suggesting that all 5 parameters are locally identifiable. On the other hand, the large spectrum of eigenvalues will affect our ability to estimate the parameters, as discussed in the next sections.

Scenario 3: The 5 parameters are not identifiable (FIM rank of 3) but the physical interpretation of the null-eigenvectors is not straightforward, unlike in Scenario 1.

Scenario 4: the FIM has full rank and narrower eigenvalue spectrum, suggesting perfect identifiability.

We explore these scenarios further in the next section through MAP parameter estimation.

5.1.2. MAP Identifiability—We recover $\mathbf{y}^*$ from $\bar{\mathbf{d}} = \mathbf{G}(\mathbf{y}^*)$ using 50 optimization runs, each characterized by a uniformly sampled initial guess from the ranges $R_{tot} = [2.0, 4.0]$, $\boldsymbol{\tau} = [0.5, 3.0]$, $(C_1/C_2) = [0.1, 10.0]$, $(R_1/R_2) = [0.1, 2.0]$, $(R_3/R_2) = [0.1, 1.0]$. We denote each optimal estimate as $\bar{\mathbf{y}}_I$, $i = 1, \ldots, 50$ and, in Figure 5, report the optimal log-likelihood and the $\overline{F}_2$ distance in parameter space between $\bar{\mathbf{y}}_i$ and $\mathbf{y}^*$ for scenarios 2, 3 and 4.

Optimal parameter locations appear dispersed in the ($log\, \mathcal{L}_{\bar{\mathbf{y}}}(\bar{\mathbf{d}})$, d_y) plane for scenario 2, suggesting the presence of multiple local minima (Figure 5). None of these minima, however, is able to reproduce accurately the target set of parameters. MAP convergence profiles for scenario 2 are also characterized by an initial steep descent followed by several iterations with relatively small improvements, suggesting the presence of ridges in the log-likelihood function. When the current optimum reaches these locations, only limited improvement is obtained even after substantially increasing the number of iterations, as confirmed by our tests using 2000 and 5000 iterations. This situation was revealed by near singularity of the FIM and a corresponding wide eigenvalue spectrum. Finally, we note that by selecting the parameter set $\bar{\mathbf{y}}_s$ characterized by $s = \text{argmax}_j\, log\, \mathcal{L}_{\bar{\mathbf{y}}_j}(\bar{\mathbf{d}})$, one can get close to the true sets of RCRCR parameters in scenario 2, as shown in Figure 5.

In scenario 3, 5 parameters need to be estimated from only 3 measurements. In this case, multiple parameter combinations (with variable distances d_y) lead to a zero log-likelihood, confirming the intuition provided by the rank of the FIM. In other words, multiple non-identifiable combinations of parameters are determined that generate the same measurement vector $\bar{\mathbf{d}}$.

Finally, all the estimated parameter sets match the true set in Scenario 4 (perfect identifiability), where optimization profiles confirm the convexity of the log-likelihood function.

5.1.3. Bayesian parameter estimation—Figure 6 illustrates the GR statistics, showing a rapid convergence of DREAM for all 3 scenarios. As expected, scenario 4 produces the

best results characterized by unimodal marginal distribution and small variance. Results in terms of 95% confidence intervals are also illustrated in Table VII.

The ability of MCMC to learn the parameters under various scenarios is quantified using

$$\theta = 1 - \sqrt{\frac{\mathbb{V}[y_j|\mathbf{d}]}{\mathbb{V}[y_j]}}, \quad (9)$$

where $\mathbb{V}[y_j|\mathbf{d}]$ denotes the marginal posterior variance for parameter y_j while $\mathbb{V}[y_j]$ denotes its prior marginal variance. When the prior variance is not effectively reduced by conditioning the model results to the available observations, the ratio $\mathbb{V}[y_j|\mathbf{d}]/\mathbb{V}[y_j] \approx 1$ and limited learning ($\theta \approx 0$) is achieved. Conversely, satisfactory learning ($\theta \approx 1$) characterizes situations, where the posterior marginal variance is reduced to a small fraction of its prior counterpart. We compute $\mathbb{V}[y_i] = \frac{1}{12}(b-a)^2$, that is, the variance of a uniform random variable in the interval [a, b].

Resulting values of θ for (R_{tot}, τ, C_1/C_2) in Table VII show effective learning even for the less identifiable scenarios 2 and 3. In scenario 3, clearly unidentifiable as discussed in Section 5.1.2, relatively large values of θ are obtained for C_1/C_2 due to the high sensitivity of $P_{0,max}$ to this quantity (Figure 4). Learning for R_{tot} is however limited, while practically no variance reduction is observed for τ. Finally, we note that the true value of R_1/R_2 is outside the 95% confidence interval in scenario 3 consistent with the singularity in the FIM.

5.2. Full Norwood model with virtual targets

After discussing the results of identifiability and parameter estimation on a simplified and reduced model to develop intuition, we proceed by applying the same tools to a complete Norwood model. We start by studying the conditions for *structural* identifiability and parameter estimation, trying to retrieve a known set of parameters (Table VIII) from virtual measurements generated through model solutions.

5.2.1. Local Identifiability—The null FIM eigenvectors with dominant components (i.e., a single component close to one and all others with a value close to zero) were employed to determine unimportant parameters. Using this approach, the initial conditions Q_{av}, P_{ubv}, Q_{uba}, P_{uba}, P_{lung}, P_{pv}, Q_{pa}, P_{pa} were removed from the parameter set, resulting in a FIM containing 32 parameters with rank 21. The remaining parameters were grouped according to anatomical proximity. Those in the atrium, $t_{1,r}$, $t_{sas,r}$, $V_{sa,0}$, d_{sa}, c_{sa}, C_{sa}, were first removed, resulting in a FIM of dimension 26,still with rank 21. We then removed the ventricle parameters $t_{svs,r}$, $V_{sv,0}$, d_{sv}, c_{sv}, b, a, leading to a 20-dimensional FIM with rank 19. A full rank 15-dimensional FIM is obtained by finally removing the parameters R_{myo}, α, β, K_{ao}, C_{ao}.

From the above changes of the FIM rank, one should conclude that the parameters in the heart model play an important role in the identification of the full LPN system, and that

specification of prior information on those parameters will likely improve the overall estimation process. To further highlight this point, in the next section, we show the effects of removing atrial and ventricular model parameters on MAP estimation.

5.2.2. MAP Identifiability—MAP estimation is performed without the unimportant initial conditions found in the previous section, by first removing the atrial parameters followed by those remaining in the heart sub-model. Figure 7 shows that the optima progressively shifts towards the origin of the ($log\, \phi_{\mathbf{y}}(\bar{\mathbf{d}})$, d_y) plane. While a trend of improved identifiability (decreasing distance from the origin) is noticed by progressively removing atrial and ventricular model parameters, all three conditions behave similarly to scenario 2 in Figure 5.

5.2.3. Bayesian parameter estimation—Optimal parameter estimates are computed first using DREAM, and successively performing NM optimization with initial guess at the parameter location with maximal posterior. The agreement between measured and predicted clinical targets and parameters is reported in Tables IX and X, respectively.

While the agreement on the clinical targets is remarkably good, not all parameters are identified equally well. Parameters with normalized distance from their true value less than about 10% are highlighted in Table X. In particular, good agreement is obtained for the ventricular unstressed volume $V_{sv,0}$, aortic compliance C_{ao}, shunt diameter D_{sh} and for most of the systemic and pulmonary circulation parameters. It also suggests that changes in combinations of atrial and ventricular model parameters may be performed without significantly altering the targets, that is, that the atrial and ventricular parameters appear to be the source of non-identifiability in the model.

Finally, Figures 8 and 9 confirm that the estimated time histories of pressure and flow rate are in good agreement with the true virtual patient physiology, the most significant difference being in the unstressed atrial volume. This will be further discussed in Section 5.3.3, where we show that preliminary estimation on a sub-model is essential to significantly improve the learning factor θ for $V_{sa,0}$ in four patient-specific simulations.

5.3. Parameter estimation with patient specific targets

From the results in the previous sections, it is apparent that estimation of the heart sub-model parameters is particularly challenging. This is due to several factors: the heart sub-model contains a relatively large number of parameters, it is the primary source of non-linearities (heart contraction mechanism and unidirectional flow in valves) and only a few targets are available for the atrial compartment.

To improve parameter estimation in this sub-system, we therefore create a sub-model isolating the heart from the other LPN components, with prescribed venous and aortic flow conditions at the boundary. We then study separate identification properties in the heart and full Norwood models and finally show that the best results are provided by a multi-level Bayesian estimation approach.

5.3.1. Parameter estimation for patient specific heart sub-models—FIM analysis on the heart sub-model reveals unimportant initial conditions Q_{av}, P_{ao}, V_{sa}, V_{sv}, and AV

inductance parameter β, resulting in an 18-dimensional FIM with rank 7. Further reduction in the number of parameters is not possible as no clear patterns are identified from the FIM null eigenvectors.

Parameter distributions are then estimated using DREAM with typical GR convergence shown in Figure 10. Estimated marginal distributions are shown in Figure 11, highlighting corresponding prior ranges. The aortic compliance C_{ao} shows a significant reduction in variance for all patients. This is likely due to the abundance of target quantities available in the proximity of the aortic capacitor (i.e., cardiac output, minimum, average and maximum aortic pressures). Values of C_{ao} estimated by DREAM were also found to be compatible to those determined from manual tuning in previous work from our research group [57].

The variance of the unstressed atrial volume $V_{sa,0}$ is also significantly reduced in all patients, in contrast to what was observed with the full model. This mainly relates to the limited variability in the venous flow rate, that is prescribed through its Fourier coefficients, unlike in full circulation models. On the other hand, it is also likely that excessive prior ranges were adopted in this case, although justified by atrial dilation typically observed in single-ventricle patients [58].

Patient UM10 is the only one with AV valve regurgitation with a non-zero k_{bw}, the regurgitant AV valve area ratio. Patient UM5 shows variability in the AV resistance coefficient a and time delay parameter $t_{d,1}$. A marked variability in $t_{d,1}$ only observed in this patient suggests possible inconsistency between the prescribed venous and aortic flow rates and will be further discussed in Section 5.3.3.

A heat map representation of the correlations between heart model parameters is illustrated in Figure 12. An inverse correlation is observed between c_{sa} and d_{sa} in the atrium similarly to c_{sv} and d_{sv} in the ventricle. An increase in c_{sa} leads to an increased passive atrial pressure at a given target volume that may be reversed by decreasing the exponent d_{sa}. All models also show a direct correlation between $V_{sa,0}$ and d_{sa} and an inverse correlation between $V_{sa,0}$ and C_{sa}, as the heart sub-model reacts to an increase in $V_{sa,0}$ by increasing d_{sa} and decreasing C_{sa} to satisfy the average and maximum atrial pressure targets. All models also show direct correlation between $V_{sv,0}$ and b, while there is little correlation between $V_{sv,0}$ and a. This shows that changes in the active pressure negative curvature are less effective in reproducing the measured heart physiology than changes in its slope, governed by the 2 parameters $V_{sv,0}$ and b. Finally, the AV compliance C_{ao} is correlated to the input and output flow time delay $t_{d,1}$, because of their proximity in the circulation layout.

5.3.2. Single-level estimation for patient specific Norwood circulation models

—A small variance is consistently obtained in the aortic compliance C_{ao} for the full LPN model (results for single-level estimation are not shown), similar to what was observed in the heart sub-model. The absence of a prescribed aortic flow rate is, in this case, compensated by the addition of CO as a target. Conversely, as previously observed under virtual patient conditions, unstressed atrial volume variability increases. Also, consistent with the heart sub-model, a large variability persists for the AV resistance coefficients a in patient UM5.

The shunt diameter D_{sh}, not included in the heart sub-model, is also associated with a limited variance, with values of 3.0470 ± 0.0379 mm for patients MUSC7, 3.4633 ± 0.0322 mm for GOSH22, 3.0744 ± 0.0360 mm for UM5 and 3.4046 ± 0.0404 mm for UM10, compatible with the shunt diameters that were implanted during Norwood surgery, that is, 4.0 mm, 3.5 mm, 4.0 mm and 4.0 mm for patients MUSC7, GOSH22, UM5 and UM10, respectively. This is consistent with expectations, as the shunt lumen diameter is known to progressively shrink following implantation due to endotheliaization.

The systemic circulation block is similarly identified for all four patients, where proximal, intermediate and distal resistances are consistently determined with a relative order $R_1 > R_2 > R_3$ (Figure 13). These values seem to be affected by the different targets (SDMA peaks and CO, respectively) specified for the venous and systemic flows. Thus, the identified parameters suggest that an *arteries+capillaries - small veins - great veins* model explains the target quantities better than an *arteries - capillaries - veins* model when the systemic circulation is simulated using three resistors. Similarly, estimation does not consistently identify a predominant compliance between C_1 and C_2. Resistance and compliance parameters in the pulmonary circulation block behave differently from those in the systemic block, likely due to the presence of additional elements, the linear and non linear shunt resistances R_{sh}, K_{sh} and the pulmonary compliance C_p. Also, maximum and minimum pulmonary pressure measurements are prescribed at these locations, while no measurements are provided for the systemic block other than the Q_p/Q_s ratio and the systemic venous return flow rate at SDMA locations.

5.3.3. Multi-level estimation for patient specific Norwood circulation models— Multi-level Bayesian estimation results for marginal parameter posteriors and parameter correlations are shown in Figures 13 and 14, respectively. A large variance in α (the AV resistance coefficient) for patient UM5 is consistently estimated from heart and Norwood models. As patient UM5 has the largest AV area, α needs to be increased to produce similar AV resistances as in other patients. This effect is amplified by the squared inverse dependence between resistance and area. Higher variability in the time delay $t_{d,1}$ for this patient also highlights a lack of compatibility between the clinically measured aortic and venous flow curves.

The adoption of prior parameter knowledge from the heart sub-model has improved the estimation of the parameters and decreased the resulting variance. Table XI shows the average parameter learning factors θ for all patients. The multi-level estimator consistently results in reduced variance and parameter learning is significantly improved by this approach. The value of θ averaged across all parameters and patients improves from 0.28 to 0.39 using a multi-level instead of a single-level approach. Moreover, some parameters can only be determined using a multi-level approach. For example, the learning factor improves from 0.04 to 0.84 for $V_{sa,0}$, and from 0.03 to 0.33 for $t_{1,r}$ (Table XI).

5.3.4. Optimal patient-specific circulation models—Optimal parameter estimates under multi-level estimation produce realistic physiology and closely approximate patient-specific targets as shown in Tables XII and XIII. Figure 15 shows the AV flow rate for patient UM10, characterized by the expected retrograde behavior during ventricular systole

as a result of valve regurgitation. The computed mean regurgitant flow rate Q_{reg} agrees well with clinical measurements, and the two positive peaks in Q_{av}, that is, filling and atrial contraction, are consistent with literature findings for single ventricle patients [58]. Pulmonary and caval vein flows show retrograde behavior during atrial contraction, consistent with the MRI flow profiles measured on the patients. Realistic tracings with correct relative timings are also observed for atrial, ventricular and aortic pressures.

Computed atrial pressure-volume loop (PV-loops) for all patients (Figure 16) are consistent with the underlying model formulation, where hysteresis characterizes atrial contraction and is absent during filling. Also, atrial volumes in patient UM10 are notably larger than in other patients with comparable BSA, possibly as a result of AV valve regurgitation in this patient (see, e.g., [59]).

Ventricular PV-loops show volume ranges and max pressures in perfect agreement with the clinical data, indicating that ventricle-arterial coupling is properly modeled by the proposed lumped parameter formulation. All patients except UM10 are characterized by ventricular PV-loops with isovolumic contraction and relaxation. Conversely, patient UM10 does not exhibit the typical isovolumic behavior due to AV valve regurgitation, and maximum ventricular pressure is higher than in other patients.

6. Conclusions

This work focuses on automatic estimation of Norwood circulation model parameters, and on how uncertainty in the clinical data collection affects these estimates. We argue that quantifying variability in the model parameters is key to characterizing the confidence in the numerical predictions produced by these models. However, this variability is typically neglected in manual tuning, resulting in deterministic parameters with no associated measures of confidence.

We considered three model formulations of increasing complexity, starting from a typical peripheral circulation circuit and progressing to a full Norwood circulation model. We combined tools from identifiability analysis and Bayesian estimation to reduce the variance in the estimated parameters and to maximize the physiological consistency of predicted physiologies.

We first conclude that a preliminary identifiability analysis is an important prerequisite to maximize predictive ability. Complex models with an excessive number of parameters may offer a detailed description of certain physiological mechanisms, but may pose identifiability challenges when trying to reproduce the response of specific patients. Using the methodologies discussed in the paper, one can seek an optimal combination of parameters and target quantities with significant benefits for automatic parameter estimation.

Second, we have shown that multi-level Bayesian estimation takes advantage of the compartmental nature of LPN circulation models, leading to a reduction in the variance of the estimated parameters, and a corresponding improvement in the *learning factor* θ across all analyzed patients. Moreover, this approach is essential for effective learning of certain parameters, particularly the unstressed atrial volume $V_{sa,0}$. Estimates of aortic compliance

C_{ao}, BT-Shunt diameter D_{sh} and systemic compliances/resistances ratios showed a particularly limited variance across all patients and MAP parameter estimates reproduced well the target clinical measurements, as shown in Table XII and XIII.

This study also confirms that proximity, in the LPN circuit, between the target clinical measurements and the parameters to estimate is beneficial and generally leads to a reduction in the estimated parameter variance.

Moreover, the randomized exploration of the parameter space provided by DREAM is important to find a robust initial guess for optimization algorithms, preventing convergence to local maxima.

Future work will be devoted to development of hemodynamic surrogates of the three-dimensional vasculature, to extend this parameter learning framework to patient-specific multiscale models. Also, further investigation on optimal model complexity will be required to understand the potential of improving parameter estimates by looking at an ensemble of circulation models.

Acknowledgments

The authors would like to thank the three anonymous Reviewers for their generous comments and feedback that greatly contributed to improve the consistency and quality of the present contribution. This work was supported by American Heart Association Grant #15POST23010012 (Daniele Schiavazzi) and by the Leducq Foundation as part of a Transatlantic Network of Excellence for Cardiovascular Research, a Burroughs Wellcome Fund Career award at the Scientific Interface, NSF CAREER OCI-1150184 (Alison Marsden) and used computational resources from the Extreme Science and Engineering Discovery Environment (XSEDE), supported by National Science Foundation grant number ACI-1053575. We also acknowledge the open source SimVascular project at www.simvascular.org.

Appendix

A.1. Heart model equations

The pressure-volume relationships in the atrial and ventricular chambers are formulated using a combination of activation function, active and passive curves, characterized by the expressions [2, 28]:

$$\begin{aligned} P_{\mathrm{sa,act}} &= \frac{(V_{\mathrm{sa}} - V_{\mathrm{sa},0})}{C_{\mathrm{sa}}}, \\ P_{\mathrm{sa,pas}} &= c_{\mathrm{sa}} \left[e^{d_{\mathrm{sa}}(V_{\mathrm{sa}} - V_{\mathrm{sa},0})} - 1 \right], \\ P_{\mathrm{sv,act}} &= a[(V_{\mathrm{sv}} - V_{\mathrm{sv},0}) + b](V_{\mathrm{sv}} - V_{\mathrm{sv},0}), \\ P_{\mathrm{sv,pas}} &= c_{\mathrm{sv}} \left[e^{d_{\mathrm{sv}}(V_{\mathrm{sv}} - V_{\mathrm{sv},0})} - 1 \right], \\ P_{\mathrm{sv}} &= A_V P_{\mathrm{sv,act}} + P_{\mathrm{sv,pas}}, \\ P_{\mathrm{sa}} &= A_A P_{\mathrm{sa,act}} + P_{\mathrm{sa,pas}}, \end{aligned} \tag{A.1}$$

where $P_{sa,act}$, $P_{sa,pas}$ are the active and passive pressure curves for the atrium, while $P_{sv,act}$, $P_{sv,pas}$ refer to the ventricle. The quantities A_v, A_a are the ventricular and atrial activation functions, expressed by

$$A_V = \begin{cases} \left[1 - \cos\left(\frac{2\pi t_{\mathrm{mv}}}{t_{\mathrm{svs}}}\right)\right]/2, & \text{if} t_{\mathrm{mv}} < t_{\mathrm{svs}} \\ 0, & \text{otherwise} \end{cases}$$
$$A_A = \begin{cases} \left[1 - \cos\left(\frac{2\pi t_{\mathrm{ma}}}{t_{\mathrm{sas}}}\right)\right]/2, & \text{if} t_{\mathrm{ma}} < t_{\mathrm{sas}} \\ 0, & \text{otherwise} \end{cases} \quad \text{(A.2)}$$

where t_{ma} and t_{mv} are relative cycle-times measured from the beginning of atrial and ventricular activation and t_{svs} and t_{sas} the total ventricular and atrial activation times, respectively. The aortic valve is regulated by the pressure difference between the ventricle and ascending AO. The left ventricular outflow (LVOF) is computed from the following equation:

$$\mathrm{LVOF} = \begin{cases} \frac{-R_{\mathrm{myo}} + \sqrt{R_{\mathrm{myo}}^2 + 4.0 K_{\mathrm{ao}}(P_{\mathrm{sv}} - P_{\mathrm{ao}})}}{2.0 K_{\mathrm{ao}}}, & \text{if} P_{\mathrm{sv}} > P_{\mathrm{ao}} \\ 0, & \text{otherwise} \end{cases} \quad \text{(A.3)}$$

The effective pressure in the left ventricle that accounts for the pressure drop due to the viscous resistance in the myocardium is evaluated as [2, 28]:

$$P_{\mathrm{sv,eff}} = P_{\mathrm{sv}} - R_{\mathrm{myo}} \cdot \mathrm{LVOF}. \quad \text{(A.4)}$$

The AV valve is simulated as an assembly of one resistance and one inductance [60], where the two parameters α and β are used to better capture the shape of the AV flow rate curve, characterized by a first peak with the atrium behaving as a reservoir/conduit and a second peak characterized by atrial contraction

$$K_{\mathrm{av}} = \alpha \cdot \frac{\mathrm{NUM}}{A_{\mathrm{fw}}^2}, \quad L_{\mathrm{av}} = \beta \cdot \sqrt{\frac{\mathrm{NUM}}{A_{\mathrm{fw}}}}. \quad \text{(A.5)}$$

where the factor NUM takes into account the conversion between units and other constants and A_{fw} is reported in Table III for the selected patients.

Flow in the AV valve is described by the equation

$$\frac{dQ_{\mathrm{av}}}{\mathrm{dt}} = \frac{P_{\mathrm{sa}} - P_{\mathrm{sv}} - K_{\mathrm{av}} Q_{\mathrm{av}} |Q_{\mathrm{av}}|}{L_{\mathrm{av}}}, \quad \text{(A.6)}$$

where the AV flow Q_{av} is prevented from assuming negative values for cases where no valve regurgitation is observed. The model is completed by the following three equations

$$\begin{aligned}\frac{dV_{\mathrm{sv}}}{\mathrm{dt}}&=Q_{\mathrm{av}}-\mathrm{LVOF},\\ \frac{dV_{\mathrm{sa}}}{\mathrm{dt}}&=Q_{\mathrm{ven}}-Q_{\mathrm{av}},\\ \frac{dP_{\mathrm{ao}}}{\mathrm{dt}}&=\frac{\mathrm{LVOF}-Q_{\mathrm{ao}}}{C_{\mathrm{ao}}}.\end{aligned} \tag{A.7}$$

The cardiac cycle is assumed to start at the onset of ventricular activation. As MRI clinical measurements of venous and aortic flow rates may not be synchronized with this choice, we adopt an additional parameter $t_{d,1}$ accounting for the possible time delay between the prescribed flow curves (assumed synchronous) and the simulated heart cycle.

Finally, we again stress that the heart model is non linear, due to the activation mechanism in the heart contraction and unidirectional flow in the valves.

A.2. Peripheral circulation model equations

Circulatory blocks in the upper/lower body and in the lungs were modeled by RLC-R-CR blocks (Figure 1(c)). In the pulmonary block, the flow rate through the lungs and time variation of incoming pulmonary flow rate and lung pressure is described by

$$\begin{aligned}Q_{\mathrm{lung}}&=\frac{P_{\mathrm{lung}}-P_{\mathrm{pv}}}{R_{2,\mathrm{PVR}}},\\ \frac{dQ_{\mathrm{pa}}}{\mathrm{dt}}&=\frac{P_{\mathrm{pa}}-Q_{\mathrm{pa}}R_{1,\mathrm{PVR}}-P_{\mathrm{lung}}}{L_{\mathrm{PVR}}},\\ \frac{dP_{\mathrm{lung}}}{\mathrm{dt}}&=\frac{Q_{\mathrm{pa}}-Q_{\mathrm{lung}}}{C_{1,\mathrm{PVR}}}+\mathrm{DPith}.\end{aligned} \tag{A.8}$$

Similarly, the following equations describe the venous side of the pulmonary circulation:

$$\begin{aligned}Q_{\mathrm{vp}}&=\frac{P_{\mathrm{pv}}-P_{\mathrm{sa}}}{R_{3,\mathrm{PVR}}}\\ \frac{dP_{\mathrm{pv}}}{\mathrm{dt}}&=\frac{Q_{\mathrm{lung}}-Q_{\mathrm{vp}}}{C_{2,\mathrm{PVR}}}+\mathrm{DPith},\end{aligned} \tag{A.9}$$

while evolution in time of flow rate and pressure in the systemic block are instead:

$$\begin{aligned}\frac{dQ_{\mathrm{uba}}}{\mathrm{dt}}&=\frac{P_{\mathrm{ao}}-P_{\mathrm{uba}}-R_{1,\mathrm{SVR}}Q_{\mathrm{uba}}-k_{s,\mathrm{UB}}Q_{\mathrm{uba}}^2}{L_S\mathrm{VR}},\\ Q_{\mathrm{ub}}&=\frac{P_{\mathrm{uba}}-P_{\mathrm{ubv}}}{R_{2,\mathrm{SVR}}},\\ Q_{\mathrm{ubv}}&=\frac{P_{\mathrm{ubv}}-P_{\mathrm{sa}}}{R_{3,\mathrm{SVR}}},\\ \frac{dP_{\mathrm{uba}}}{\mathrm{dt}}&=\frac{Q_{\mathrm{uba}}-Q_{\mathrm{ub}}}{C_{1,\mathrm{SVR}}},\\ \frac{dP_{\mathrm{ubv}}}{\mathrm{dt}}&=\frac{Q_{\mathrm{ub}}-Q_{\mathrm{ubv}}}{C_{2,\mathrm{SVR}}}.\end{aligned} \tag{A.10}$$

Conservation of mass in the atrium and ventricle are expressed as:

$$\begin{aligned}\frac{dV_{\mathrm{sv}}}{\mathrm{dt}}&=Q_{\mathrm{av}}-Q_{\mathrm{ao}},\\ \frac{V_{\mathrm{sa}}}{\mathrm{dt}}&=Q_{\mathrm{ubv}}+Q_{\mathrm{vp}}-Q_{\mathrm{av}},\end{aligned}\quad \text{(A.11)}$$

and, finally, aortic and pulmonary artery compliance are accounted using the following relationship:

$$\begin{aligned}\frac{dP_{\mathrm{ao}}}{\mathrm{dt}}&=\frac{Q_{\mathrm{ao}}-Q_{\mathrm{sh}}-Q_{\mathrm{uba}}}{C_{\mathrm{ao}}}+\mathrm{DPith}\\ \frac{dP_{\mathrm{pa}}}{\mathrm{dt}}&=\frac{Q_{\mathrm{sh}}-Q_{\mathrm{pa}}}{\mathrm{Cp}}+\mathrm{DPith}.\end{aligned}\quad \text{(A.12)}$$

In this study the effect of the respiration is neglected, therefore we set *DPith* = 0.

A.3. Non linear shunt resistance

The aorto-pulmonary shunt is modeled using a non linear pressure-flow rate relationship of the form [28]:

$$\begin{aligned}P_{\mathrm{ao}}-P_{\mathrm{pa}}&=R_{\mathrm{sh}}Q_{\mathrm{sh}}+K_{\mathrm{sh}}Q_{\mathrm{sh}}^2, \quad \text{leading to}\\ Q_{\mathrm{sh}}&=\frac{-R_{\mathrm{sh}}+\sqrt{R_{\mathrm{sh}}^2+4K_{\mathrm{sh}}(P_{\mathrm{ao}}-P_{\mathrm{pa}})}}{2K_{\mathrm{sh}}}.\end{aligned}\quad \text{(A.13)}$$

The linear and non-linear pressure loss coefficients R_{sh} and K_{sh}, are expressed as a function of the shunt diameter D_{sh}, through the following empirical relationships:

$$R_{\mathrm{sh}}=\frac{k_1}{D^4}\quad \text{and}\quad K_{\mathrm{sh}}=\frac{k_2}{D^4}\ , \quad \text{(A.14)}$$

where k_1 and k_2 are proportionality constants, which can be derived experimentally or computationally; k_1 is dependent on shunt length and blood viscosity, and k_2 depends on local geometry (shunt angle of insertion, length, and subclavian and pulmonary arterial diameters). In this study, k_1 and k_2 values were set as 960 and 5200 mmHg l min^{-2} mm^4, as in [28].

A.4. Fourier coefficients for aortic and venous flow rates

The Fourier coefficients used to prescribe aortic and venous flow rates are reported in this section, for the heart model under real and virtual patient conditions. The current simulation time is denoted with t_k, while a time delay $t_{d,1}$ is introduced to account for possible shifts between the onset of ventricular contraction in the heart sub-model and the time origin used during MRI acquisitions, that is,

$$t_k^* = t_k + t_{d,1}. \quad \text{(A.15)}$$

We set the fundamental frequency equal to $\omega = 2{:}0\ \pi/t_c$ with t_c the heart cycle time, and compute the venous flow rate as follows:

$$\begin{aligned} Q_{\text{ven}} &= a_{in,9} + \sum_{i=1}^{8} a_{\text{in},i}\cos(i\omega t_k^*) + b_{\text{in},i}\sin(i\omega t_k^*), \\ Q_{\text{ao}} &= a_{\text{out},9} + \sum_{i=1}^{8} a_{\text{out},i}\cos(i\omega t_k^*) + b_{\text{out},i}\sin(i\omega t_k^*), \end{aligned} \quad \text{(A.16)}$$

Numerical values of $a_{in,i}$, $a_{out,i}$, $b_{in,i}$ and $b_{out,i}$ for both real and virtual patient conditions, are reported in Table A.1, A.2 and A.3.

Table A.1

Fourier coefficients for prescribed aortic and venous flow in the heart sub-model for patient MUSC7 and GOSH22.

	Aortic flow rate			Venous flow rate	
Coefficient	**MUSC7**	**GOSH22**	**Coefficient**	**MUSC7**	**GOSH22**
$a_{in,1}$	$4.21 \times 10^{+00}$	$1.26 \times 10^{+01}$	$a_{out,1}$	$2.98 \times 10^{+00}$	$-6.94 \times 10^{+00}$
$a_{in,2}$	$-1.57 \times 10^{+01}$	$-5.85 \times 10^{+00}$	$a_{out,2}$	$-2.00 \times 10^{+01}$	$-1.95 \times 10^{+01}$
$a_{in,3}$	8.73×10^{-01}	$2.26 \times 10^{+00}$	$a_{out,3}$	$-4.37 \times 10^{+00}$	$-4.98 \times 10^{+00}$
$a_{in,4}$	$1.96 \times 10^{+00}$	$5.42 \times 10^{+00}$	$a_{out,4}$	$-3.96 \times 10^{+00}$	-6.82×10^{-01}
$a_{in,5}$	-9.14×10^{-01}	$1.12 \times 10^{+00}$	$a_{out,5}$	3.37×10^{-01}	9.30×10^{-01}
$a_{in,6}$	-8.62×10^{-01}	-9.53×10^{-01}	$a_{out,6}$	$-1.41 \times 10^{+00}$	$2.62 \times 10^{+00}$
$a_{in,7}$	-7.60×10^{-01}	2.30×10^{-02}	$a_{out,7}$	4.66×10^{-01}	-3.76×10^{-01}
$a_{in,8}$	-3.59×10^{-01}	$1.70 \times 10^{+00}$	$a_{out,8}$	1.09×10^{-01}	$3.03 \times 10^{+00}$
$a_{in,9}$	$2.52 \times 10^{+01}$	$3.09 \times 10^{+01}$	$a_{out,9}$	$2.52 \times 10^{+01}$	$3.09 \times 10^{+01}$
$b_{in,1}$	8.91×10^{-01}	$8.08 \times 10^{+00}$	$b_{out,1}$	$3.87 \times 10^{+01}$	$4.49 \times 10^{+01}$
$b_{in,2}$	$1.81 \times 10^{+01}$	$1.29 \times 10^{+01}$	$b_{out,2}$	$5.51 \times 10^{+00}$	$-5.84 \times 10^{+00}$
$b_{in,3}$	$1.36 \times 10^{+01}$	$1.45 \times 10^{+01}$	$b_{out,3}$	$-2.79 \times 10^{+00}$	$-1.72 \times 10^{+00}$
$b_{in,4}$	$1.18 \times 10^{+00}$	$5.50 \times 10^{+00}$	$b_{out,4}$	$-2.69 \times 10^{+00}$	$-7.19 \times 10^{+00}$
$b_{in,5}$	-9.28×10^{-01}	$-2{:}40 \times 10^{+02}$	$b_{out,5}$	$-1.73 \times 10^{+00}$	$-1.34 \times 10^{+01}$
$b_{in,6}$	-7.00×10^{-01}	$1.28 \times 10^{+00}$	$b_{out,6}$	$-7.53 \times 10^{+01}$	$-2.50 \times 10^{+00}$
$b_{in,7}$	-7.78×10^{-01}	$2.04 \times 10^{+00}$	$b_{out,7}$	$-1.52 \times 10^{+00}$	$2.26 \times 10^{+01}$
$b_{in,8}$	-2.04×10^{-01}	$1.18 \times 10^{+00}$	$b_{out,8}$	$-1.97 \times 10^{+01}$	$9.81 \times 10^{+01}$

Table A.2

Fourier coefficients for prescribed aortic and venous flow in the heart sub-model for patient UM5 and UM10.

	Aortic flow rate			Venous flow rate	
Coefficient	**UM5**	**UM10**	**Coefficient**	**UM5**	**UM10**
$a_{in,1}$	$7.54 \times 10^{+00}$	$5.21 \times 10^{+01}$	$a_{out,1}$	$-3.36 \times 10^{+00}$	$-2.13 \times 10^{+01}$
$a_{in,2}$	$-6.66 \times 10^{+00}$	$4.15 \times 10^{+01}$	$a_{out,2}$	$-2.70 \times 10^{+01}$	$-6.09 \times 10^{+00}$
$a_{in,3}$	$9.32 \times 10+^{00}$	$-1.09 \times 10^{+01}$	$a_{out,3}$	$2.72 \times 10^{+00}$	$-5.57 \times 10^{+00}$
$a_{in,4}$	$2.71 \times 10^{+00}$	$-2.48 \times 10^{+00}$	$a_{out,4}$	$-4.47 \times 10^{+00}$	$3.53 \times 10^{+00}$
$a_{in,5}$	$-2.08 \times 10^{+00}$	$5.62 \times 10^{+00}$	$a_{out,5}$	$6.09 \times 10^{+00}$	-3.42×10^{-02}
$a_{in,6}$	6.89×10^{-01}	$-3.14 \times 10^{+00}$	$a_{out,6}$	6.24×10^{-03}	$2.06 \times 10^{+00}$
$a_{in,7}$	$1.48 \times 10-^{01}$	-7.53×10^{-01}	$a_{out,7}$	$3.61 \times 10^{+00}$	3.55×10^{-01}
$a_{in,8}$	-1.46×10^{-01}	6.09×10^{-01}	$a_{out,8}$	-8.96×10^{-01}	-3.21×10^{-01}
$a_{in,9}$	$2.70 \times 10^{+01}$	$3.10 \times 10^{+01}$	$a_{out,9}$	$2.70 \times 10^{+01}$	$3.10 \times 10^{+01}$
$b_{in,1}$	$-1.38 \times 10^{+01}$	$4.86 \times 10^{+01}$	$b_{out,1}$	$4.57 \times 10^{+01}$	$3.85 \times 10^{+01}$
$b_{in,2}$	$4.64 \times 10^{+00}$	$-1.63 \times 10^{+01}$	$b_{out,2}$	$-6.21 \times 10+^{00}$	$-1.04 \times 10^{+01}$
$b_{in,3}$	$5.27 \times 10^{+00}$	$-1.56 \times 10^{+01}$	$b_{out,3}$	$-5.34 \times 10^{+00}$	-8.66×10^{-01}
$b_{in,4}$	$-4.03 \times 10^{+00}$	$8.58 \times 10^{+00}$	$b_{out,4}$	$-4.27 \times 10^{+00}$	$-1.75 \times 10^{+00}$
$b_{in,5}$	6.40×10^{-01}	$-2.68 \times 10^{+00}$	$b_{out,5}$	$-3.46 \times 10^{+00}$	$-1.97 \times 10^{+00}$
$b_{in,6}$	9.53×10^{-01}	$-1.91 \times 10^{+00}$	$b_{out,6}$	$1.07 \times 10^{+00}$	1.06×10^{-01}
$b_{in,7}$	-4.54×10^{-01}	$2.06 \times 10^{+00}$	$b_{out,7}$	-4.04×10^{-01}	-8.59×10^{-01}
$b_{in,8}$	1.48×10^{-01}	-6.84×10^{-02}	$b_{out,8}$	$2.68 \times 10^{+00}$	$1.99 \times 10^{+00}$

Table A.3

Fourier coefficients for prescribed aortic and venous flow in the heart sub-model for virtual patient conditions.

Coefficient	Aortic flow rate Virtual Patient	Coefficient	Venous flow rate Virtual Patient
$a_{in,1}$	-5.99×10^{-01}	$a_{out,1}$	$3.64 \times 10^{+01}$
$a_{in,2}$	$1.04 \times 10^{+01}$	$a_{out,2}$	$5.57 \times 10^{+2}$
$a_{in,3}$	$1.68 \times 10^{+00}$	$_{aout,3}$	$-2.71 \times 10^{+01}$
$a_{in,4}$	$4.64 \times 10^{+00}$	$a_{out,4}$	$-3.01 \times 10^{+01}$
$a_{in,5}$	4.06×10^{-01}	$a_{out,5}$	$-1.68 \times 10^{+01}$
$a_{in,6}$	-8.77×10^{-01}	$a_{out,6}$	$-3.75 \times 10^{+00}$
$a_{in,7}$	5.77×10^{-02}	$a_{out,7}$	$1.33 \times 10^{+00}$
$a_{in,8}$	-4.66×10^{-01}	$a_{out,8}$	$1.01 \times 10^{+00}$
$a_{in,9}$	$2.63 \times 10^{+01}$	$a_{out,9}$	$2.67 \times 10^{+01}$
$b_{in,1}$	$-7.74 \times 10^{+00}$	$b_{out,1}$	$3.72 \times 10^{+01}$
$b_{in,2}$	$7.62 \times 10^{+00}$	$b_{out,2}$	$4.77 \times 10^{+01}$
$b_{in,3}$	$4.99 \times 10^{+00}$	$b_{out,3}$	$2.97 \times 10^{+01}$
$b_{in,4}$	-1.94×10^{-01}	$b_{out,4}$	$3.66 \times 10^{+00}$

Coefficient	Aortic flow rate Virtual Patient	Coefficient	Venous flow rate Virtual Patient
$b_{in,5}$	$1.68 \times 10^{+00}$	$b_{out,5}$	$-1.05 \times 10^{+01}$
$b_{in,6}$	-7.00×10^{-01}	$b_{out,6}$	$-1.02 \times 10^{+01}$
$b_{in,7}$	7.95×10^{-01}	$b_{out,7}$	$-4.43 \times 10^{+00}$
$b_{in,8}$	1.19×10^{-01}	$b_{out,8}$	-7.53×10^{-01}

References

1. Snyder M, Rideout V. Computer simulation studies of the venous circulation. IEEE Transactions on Biomedical Engineering. 1969; 16(4):325–334. [PubMed: 5354910]
2. Avanzolini G, Barbini P, Cappello A, Cevese A. Time-varying mechanical properties of the left ventricle - a computer simulation. IEEE Transactions on Biomedical Engineering. 1985; 32(10): 756–763. [PubMed: 4054920]
3. Avanzolini G, Barbini P, Cappello A, Cevenini G. CADCS simulation of the closed-loop cardiovascular system. International Journal of Bio-medical Computing. 1988; 22(1):39–49. [PubMed: 3346090]
4. Fontan F, Baudet E. Surgical repair of tricuspid atresia. Thorax. 1971; 26(3):240–248. [PubMed: 5089489]
5. Norwood WI, Lang P, Hansen DD. Physiologic repair of aortic atresia-hypoplastic left heart syndrome. The New England Journal of Medicine. 1983; 308(1):23–26. [PubMed: 6847920]
6. Malec E, Januszewska K, Kolcz J, Pajak J. Factors influencing early outcome of Norwood procedure for hypoplastic left heart syndrome. European Journal of Cardio-Thoracic Surgery. 2000; 18(2):202–206. [PubMed: 10925230]
7. Pennati G, Migliavacca F, Dubini G, Pietrabissa R, de Leval M. A mathematical model of circulation in the presence of the bidirectional cavopulmonary anastomosis in children with a univentricular heart. Medical Engineering & Physics. 1997; 19(3):223–234. [PubMed: 9239641]
8. Biglino G, Giardini A, Hsia TY, Figliola R, Taylor AM, Schievano S. MOCHA Collaborative Group. Modeling single ventricle physiology: review of engineering tools to study first stage palliation of hypoplastic left heart syndrome. Frontiers in Pediatrics. 2013; 1(31):1–9. [PubMed: 24400249]
9. DeGroff CG. Modeling the Fontan circulation: where we are and where we need to go. Pediatric Cardiology. 2008; 29(1):3–12. [PubMed: 17917765]
10. Pennati G, Migliavacca F, Dubini G, Bove E. Modeling of systemic-to-pulmonary shunts in newborns with a univentricular circulation: State of the art and future directions. Progress in Pediatric Cardiology. 2010; 30(1):23–29.
11. Ursino M. Interaction between carotid baroregulation and the pulsating heart: a mathematical model. American Journal of Physiology-Heart and Circulatory Physiology. 1998; 275(5):H1733–H1747.
12. Spilker R, Taylor C. Tuning multidomain hemodynamic simulations to match physiological measurements. Annals of Biomedical Engineering. 2010; 38(8):2635–2648. [PubMed: 20352338]
13. Revie JA, Stevenson DJ, Chase JG, Hann CE, Lambermont BC, Ghuysen A, Kolh P, Shaw GM, Heldmann S, Desaive T. Validation of subject-specific cardiovascular system models from porcine measurements. Computer Methods and Programs in Biomedicine. 2013; 109(2):197–210. [PubMed: 22126892]
14. Sughimoto K, Liang F, Takahara Y, Mogi K, Yamazaki K, Takagi S, Liu H. Assessment of cardiovascular function by combining clinical data with a computational model of the cardiovascular system. The Journal of Thoracic and Cardiovascular Surgery. 2013; 145(5):1367–1372. [PubMed: 22944091]
15. Yu Y, Boston J, Simaan M, Antaki J. Minimally invasive estimation of systemic vascular parameters. Annals of Biomedical Engineering. 2001; 29(7):595–606. [PubMed: 11501624]

16. Xiao X, Ozawa E, Huang Y, Kamm R. Model-based assessment of cardiovascular health from noninvasive measurements. Annals of Biomedical Engineering. 2002; 30(5):612–623. [PubMed: 12108836]
17. Deswysen B. Parameter estimation of a simple model of the left ventricle and of the systemic vascular bed, with particular attention to the physical meaning of the left ventricular parameters. IEEE Transactions on Biomedical Engineering. 1977; 24(1):29–38. [PubMed: 832886]
18. Clark J, Ling R, Srinivasan R, Cole J, Pruett R. A two-stage identification scheme for the determination of the parameters of a model of left heart and systemic circulation. IEEE Transactions on Biomedical Engineering. 1980; 27(1):20–29. [PubMed: 7358409]
19. Deswysen B, Charlier A, Gevers M. Quantitative evaluation of the systemic arterial bed by parameter estimation of a simple model. Medical and Biological Engineering and Computing. 1980; 18(2):153–166. [PubMed: 7392681]
20. McInnis B, Guo ZW, Lu P, Wang JC. Adaptive control of left ventricular bypass assist devices. IEEE Transactions on Automatic Control. 1985; 30(4):322–329.
21. Shimooka T, Mitamura Y, Yuhta T. Investigation of parameter estimator and adaptive controller for assist pump by computer simulation. Artificial Organs. 1991; 15(2):119–128. [PubMed: 2036060]
22. Avanzolini G, Barbini P, Cappello A. Comparison of algorithms for tracking short-term changes in arterial circulation parameters. IEEE Transactions on Biomedical Engineering. 1992; 39(8):861–867. [PubMed: 1505999]
23. Ruchti TL, Brown RH, Jeutter DC, Feng X. Identification algorithm for systemic arterial parameters with application to total artificial heart control. Annals of Biomedical Engineering. 1993; 21(3):221–236. [PubMed: 8328722]
24. Yu YC, Boston JR, Simaan MA, Antaki JF. Estimation of systemic vascular bed parameters for artificial heart control. IEEE Transactions on Automatic Control. 1998; 43(6):765–778.
25. Kung E, Baretta A, Baker C, Arbia G, Biglino G, Corsini C, Schievano S, Vignon-Clementel IE, Dubini G, Pennati G, Taylor A, Dorfman A, Hlavacek AM, Marsden AL, Hsia TY, Migliavacca F. for the Modeling Of Congenital Hearts Alliance (MOCHA)+ Investigators. Predictive modeling of the virtual hemi-Fontan operation for second stage single ventricle palliation: two patient-specific cases. Journal of Biomechanics. 2013; 46(2):423–429. [PubMed: 23174419]
26. Corsini C, Baker C, Kung E, Schievano S, Arbia G, Baretta A, Biglino G, Migliavacca F, Dubini G, Pennati G, Marsden AL, Vignon-Clementel IE, Taylor A, Hsia TY, Dorfman A. for the Modeling of Congenital Hearts Alliance (MOCHA)+ Investigators. An integrated approach to patient-specific predictive modeling for single ventricle heart palliation. Computer Methods in Biomechanics and Biomedical Engineering. 2014; 17(14):1572–1589. [PubMed: 23343002]
27. Cappello A, Cevenini G, Avanzolini G. Model selection for ventricular mechanics: a sensitivity analysis approach. Journal of Biomedical Engineering. 1987; 9(1):13–20. [PubMed: 3795899]
28. Migliavacca F, Pennati G, Dubini G, Fumero R, Pietrabissa R, Urcelay G, Bove E, Hsia T, de Leval M. Modeling of the Norwood circulation: effects of shunt size, vascular resistances, and heart rate. American Journal of Physiology-Heart and Circulatory Physiology. 2001; 280(5):H2076–H2086. [PubMed: 11299209]
29. Spilker RL, Feinstein JA, Parker DW, Reddy VM, Taylor CA. Morphometry-based impedance boundary conditions for patient-specific modeling of blood flow in pulmonary arteries. Annals of Biomedical Engineering. 2007; 35(4):546–559. [PubMed: 17294117]
30. Presson RJ, Audi S, Hanger C, Zenk G, Sidner R, Linehan J, Wagner WJ, Dawson C. Anatomic distribution of pulmonary vascular compliance. Journal of Applied Physiology. 1998; 84(1):303–310. [PubMed: 9451650]
31. Kilner P, Balossino R, Dubini G, Babu-Narayan S, Taylor A, Pennati G, Migliavacca F. Pulmonary regurgitation: the effects of varying pulmonary artery compliance, and of increased resistance proximal or distal to the compliance. International Journal of Cardiology. 2009; 133(2):157–166. [PubMed: 18722025]
32. Rychik J, Fogel M, Donofrio M, Goldmuntz E, Cohen M, Spray T, Jacobs M. Comparison of patterns of pulmonary venous blood flow in the functional single ventricle heart after operative aortopulmonary shunt versus superior cavopulmonary shunt. The American Journal of Cardiology. 1997; 80(7):922–926. [PubMed: 9382009]

33. Box G, Draper N. The Bayesian estimation of common parameters from several responses. Biometrika. 1965; 52(3-4):355–365.
34. Stewart W, Caracotsios M, Sørensen J. Parameter estimation from multiresponse data. AIChE Journal. 1992; 38(5):641–650.
35. Miao H, Xia X, Perelson A, Wu H. On identifiability of nonlinear ode models and applications in viral dynamics. SIAM Review. 2011; 53(1):3–39. [PubMed: 21785515]
36. Rothenberg T. Identification in parametric models. Econometrica: Journal of the Econometric Society. 1971; 39(3):577–591.
37. Gilks, WR., Roberts, GO. Strategies for improving MCMC. In: Gilks, WR.Richardson, S., Spiegelhalter, DJ., editors. Markov Chain Monte Carlo in Practice. Chapman & Hall; London: 1996. p. 89-114.
38. Jackman S. Estimation and inference via Bayesian simulation: An introduction to Markov chain Monte Carlo. American Journal of Political Science. 2000; 44(2):375–404.
39. Gustafson P, Gelfand A, Sahu S, Johnson W, Hanson T, Joseph L, Lee J. On model expansion, model contraction, identifiability and prior information: Two illustrative scenarios involving mismeasured variables. Statistical Science. 2005; 20(2):111–140.
40. Rannala B. Identifiability of parameters in MCMC Bayesian inference of phylogeny. Systematic Biology. 2002; 51(5):754–760. [PubMed: 12396589]
41. Haario H, Saksman E, Tamminen J. An adaptive Metropolis algorithm. Bernoulli. 2001; 7(2):223–242.
42. Haario H, Laine M, Mira A, Saksman E. DRAM: efficient adaptive MCMC. Statistics and Computing. 2006; 16(4):339–354.
43. Green P, Mira A. Delayed rejection in reversible jump Metropolis–Hastings. Biometrika. 2001; 88(4):1035–1053.
44. Andrieu C, Moulines E. On the ergodicity properties of some adaptive MCMC algorithms. The Annals of Applied Probability. 2006; 16(3):1462–1505.
45. Andrieu C, Thoms J. A tutorial on adaptive MCMC. Statistics and Computing. 2008; 18(4):343–373.
46. Gåsemyr J. On an adaptive version of the Metropolis–Hastings algorithm with independent proposal distribution. Scandinavian Journal of Statistics. 2003; 30(1):159–173.
47. Roberts G, Rosenthal J. Examples of adaptive MCMC. Journal of Computational and Graphical Statistics. 2009; 18(2):349–367.
48. Casella, G., Robert, C. Monte Carlo Statistical Methods. Springer-Verlag; New York: 2004.
49. Gelman, A., Carlin, J., Stern, H., Dunson, D., Vehtari, A., Rubin, D. Bayesian Data Analysis. Chapman & Hall/CRC Texts in Statistical Science; Boca Raton: 2013.
50. Vrugt J, Ter Braak C, Diks C, Robinson B, Hyman J, Higdon D. Accelerating Markov chain Monte Carlo simulation by differential evolution with self-adaptive randomized subspace sampling. International Journal of Nonlinear Sciences and Numerical Simulation. 2009; 10(3):273–290.
51. Storn R, Price K. Differential evolution–a simple and efficient heuristic for global optimization over continuous spaces. Journal of Global Optimization. 1997; 11(4):341–359.
52. Gelman A, Rubin D. Inference from iterative simulation using multiple sequences. Statistical Science. 1992; 7(4):457–472.
53. Laloy E, Vrugt J. High-dimensional posterior exploration of hydrologic models using multiple-try DREAM (ZS) and high-performance computing. Water Resources Research. 2012; 48(1):n/a–n/a.
54. Kirkpatrick S. Optimization by simulated annealing: Quantitative studies. Journal of statistical physics. 1984; 34(5-6):975–986.
55. Nelder J, Mead R. A simplex method for function minimization. The Computer Journal. 1965; 7(4):308–313.
56. Olsson D, Nelson L. The Nelder-Mead simplex procedure for function minimization. Technometrics. 1975; 17(1):45–51.
57. Schiavazzi DE, Kung EO, Marsden AL, Baker C, Pennati G, Hsia TY, Hlavacek AM, Dorfman AL. for the Modeling of Congenital Hearts Alliance (MOCHA) Investigators. Hemodynamic effects of left pulmonary artery stenosis after superior cavopulmonary connection: A patient-specific

multiscale modeling study. The Journal of Thoracic and Cardiovascular Surgery. 2015; 149(3): 689–696. [PubMed: 25659189]

58. Khoo N, Smallhorn J, Kaneko S, Kutty S, Altamirano L, Tham E. The assessment of atrial function in single ventricle hearts from birth to Fontan: a speckle-tracking study by using strain and strain rate. Journal of the American Society of Echocardiography. 2013; 26(7):756–764. [PubMed: 23669597]
59. Ghai A, Harris L, Harrison D, Webb G, Siu S. Outcomes of late atrial tachyarrhythmias in adults after the Fontan operation. Journal of the American College of Cardiology. 2001; 37(2):585–592. [PubMed: 11216983]
60. Yellin E, Peskin C. Large amplitude pulsatile water flow across an orifice. Journal of Dynamic Systems, Measurement, and Control. 1975; 97(1):92–95.

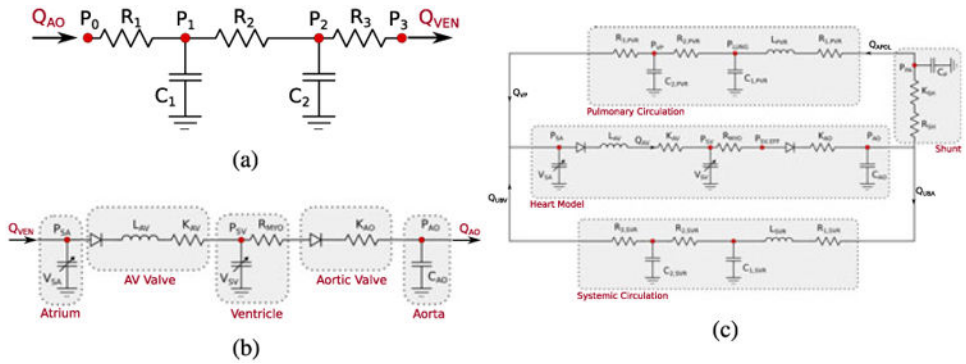

Figure 1.
(a) Schematic representation of a simple RCRCR circuit, (b) heart sub-model and (c) compete Norwood Stage I model with one systemic and one pulmonary circulation blocks.

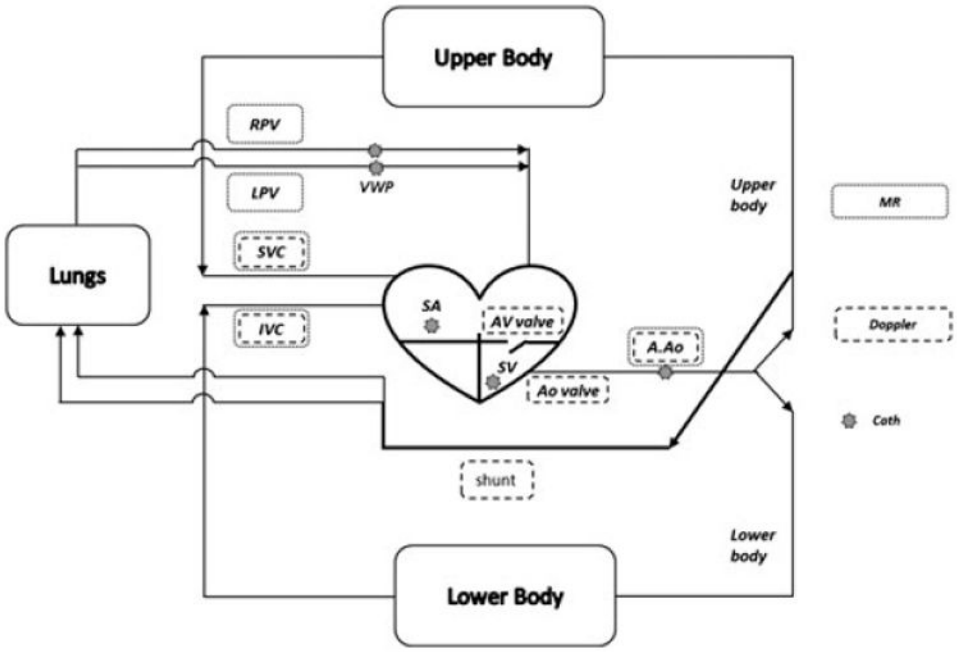

Figure 2.
Schematic layout showing the locations where MRI, echo-Doppler and catheter data was collected according to the Leducq Network protocol.

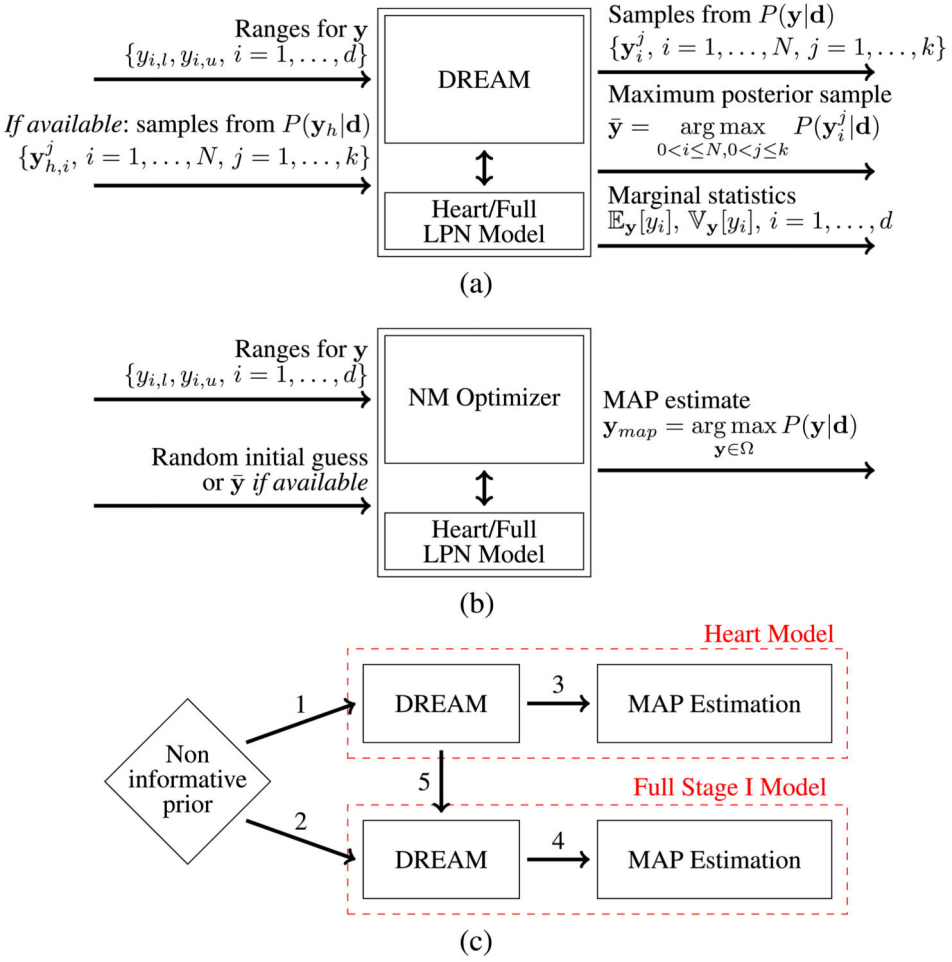

Figure 3.
Inputs and outputs for the DREAM estimation and NM optimization tasks (a and b, respectively). The adopted computational framework is also schematically represented (c). Single-level optimal parameter estimation follows the path 2–4, while multi-level estimation follows 1–5–4. Separate optimal estimation of the heart sub-model parameters can be carried out following path 1–3.

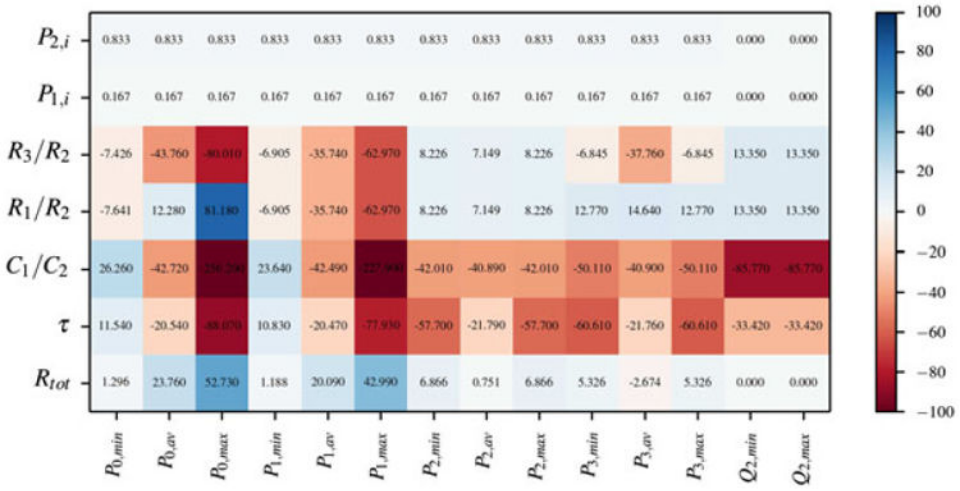

Figure 4.
Local sensitivity indexes for the RCRCR model.

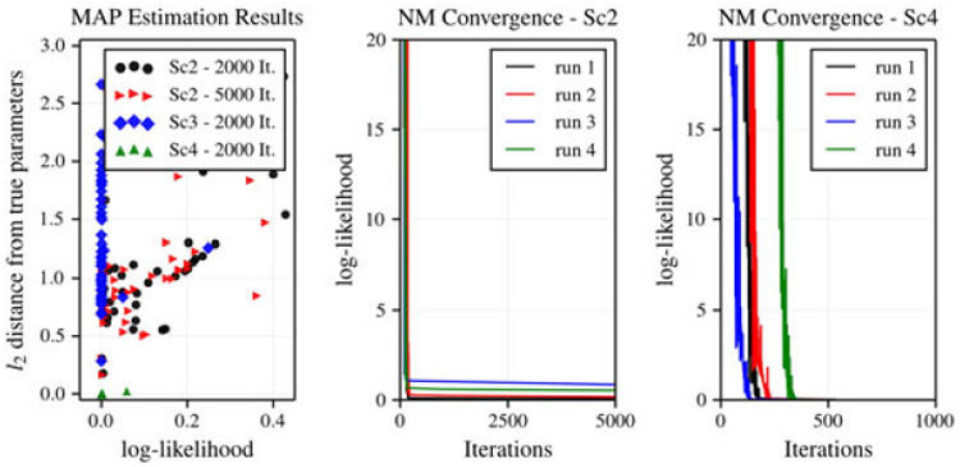

Figure 5.
MAP estimation for RCRCR model parameters under scenarios 2,3, and 4. The graph on the left shows the optimal estimates in the ($log\, \mathcal{L}_{\mathbf{y}}(\bar{\mathbf{d}})$, d_y) plane whereas likelihood convergence profiles during NM optimization are illustrated in the other two graphs for scenario 2 and 4.

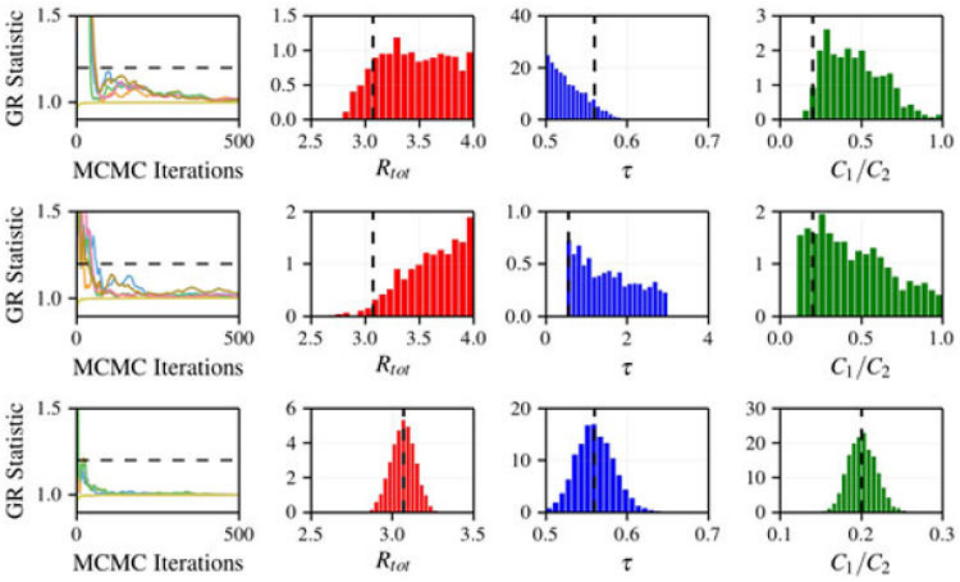

Figure 6.
Gelman-Rubin convergence and distributions of R_{tot}, τ and C_1/C_2 estimated through MCMC. Graphs in the upper row refer to scenario 2 while the central and bottom rows refer to scenario 3 and 4, respectively.

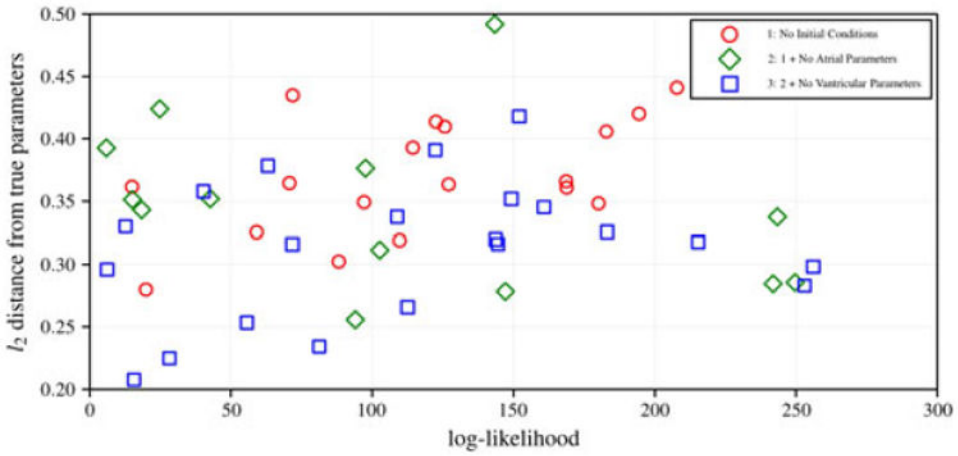

Figure 7.
Result of randomized MAP estimation on the Norwood circulation model under virtual patient conditions. While removal of the heart model parameters leads to optimal estimates closer to the origin of the ($log\ \mathcal{L}_{\mathbf{y}}(\bar{\mathbf{d}})$, d_y) plane, no distinct regimes (as in Figure 5) can be identified.

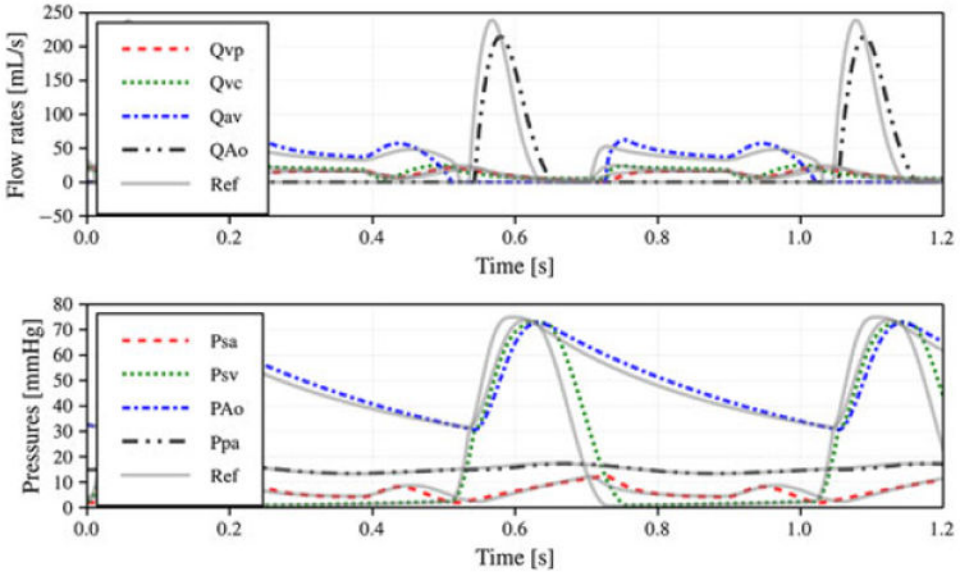

Figure 8.
Estimated and virtual patient time histories of pressure and flow rate. Estimated MAP curves are drawn using dashed lines whereas continuous curves identify reference virtual patient conditions.

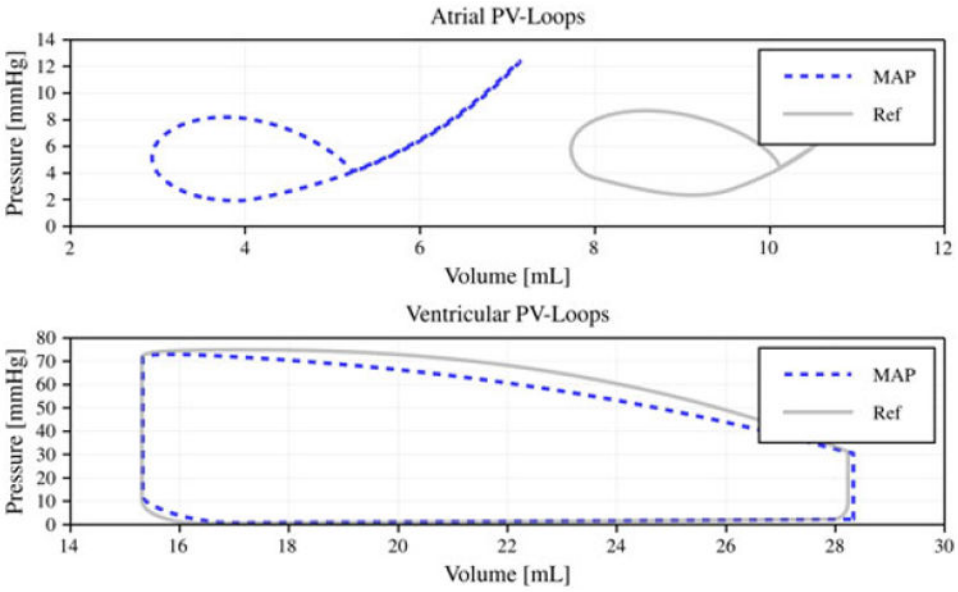

Figure 9.
Estimated and virtual patient pressure-volume loops. Estimated MAP curves are drawn using dashed lines whereas continuous curves identify reference virtual patient conditions.

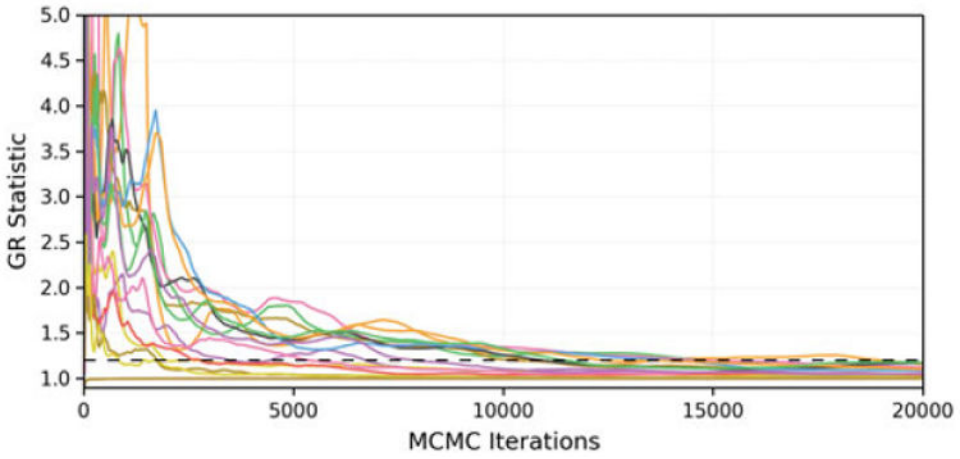

Figure 10.
Gelman-Rubin diagnostic profiles for heart sub-model parameter estimation using DREAM. A sufficient number of iterations is executed to reduce this quantity below 1.2 for each Markov chain.

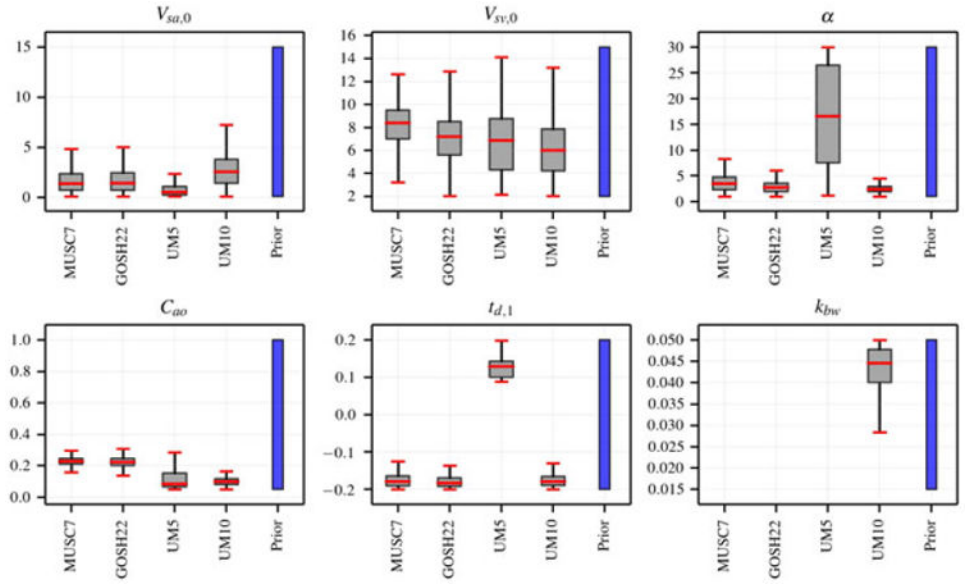

Figure 11.
Box whiskers representation of heart sub-model parameter distributions. Estimates of the unstressed volume in the atrium $V_{sa,0}$ are consistently characterized by a smaller variability than the same quantities for the ventricle $V_{sv,0}$. Values of aortic compliance C_{ao} are well indentified. Differences are observed in the prescribed inflow/outflow time shift parameter $t_{d,1}$ and atrio-ventricular resistance coefficient α for patient UM5. Finally, the ratio k_{bw} is estimated for patient UM10, the only patient with a regurgitant atrio-ventricular valve.

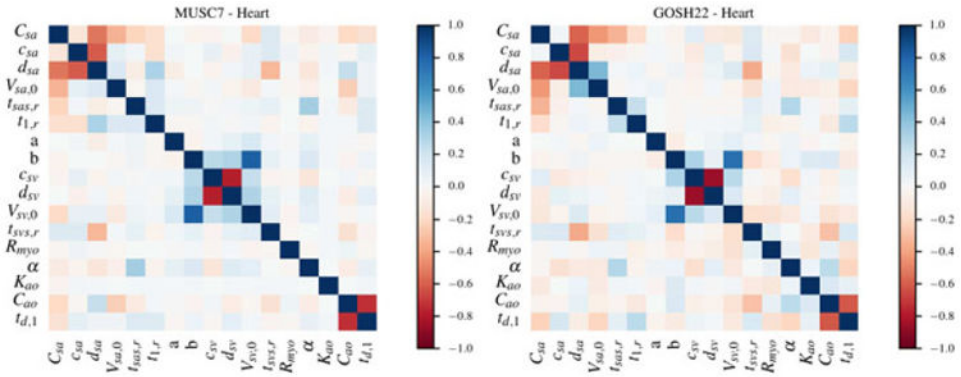

Figure 12.
MCMC parameter correlations for the heart sub-model of patients MUSC7 and GOSH22. Strong correlations can be observed between parameters belonging to the same functional compartment (e.g., atrial and ventricular model parameters).

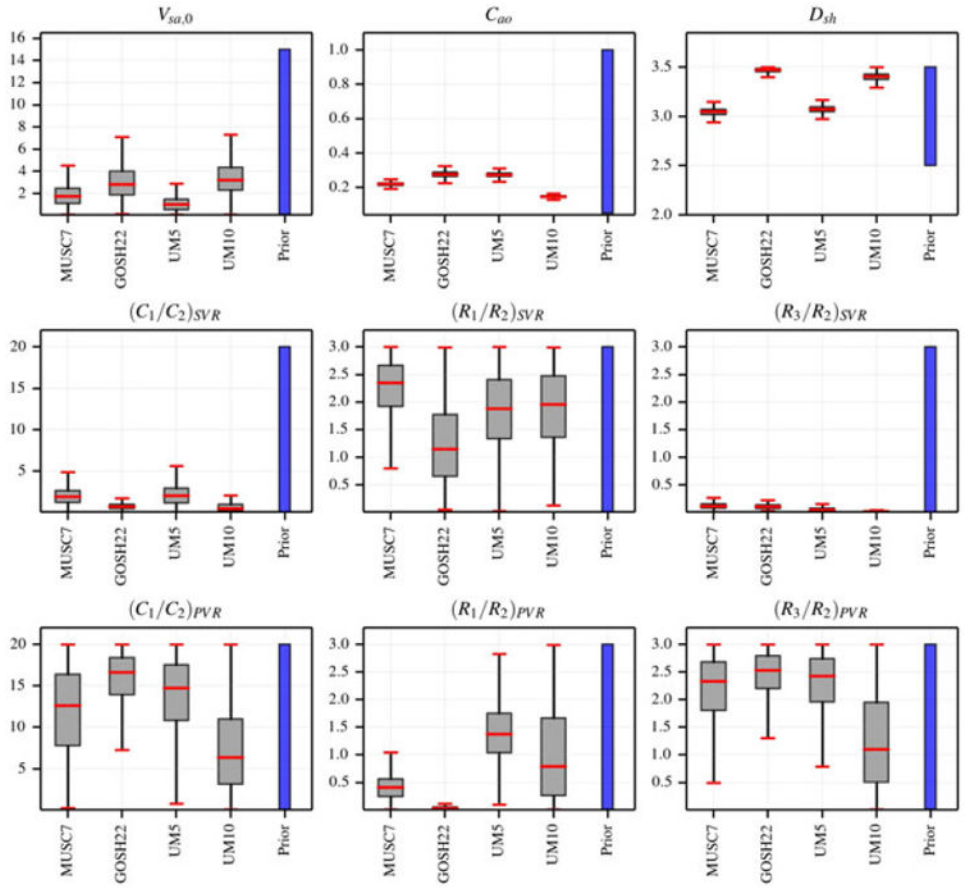

Figure 13.
Box whiskers representation of Norwood model parameters identified using multi-level adaptive MCMC. The plots show the limited variance associated with estimates of unstressed atrial volume $V_{sa,0}$, aortic compliance C_{ao}, BT-Shunt diameter D_{sh} and systemic capacitance and resistance ratios.

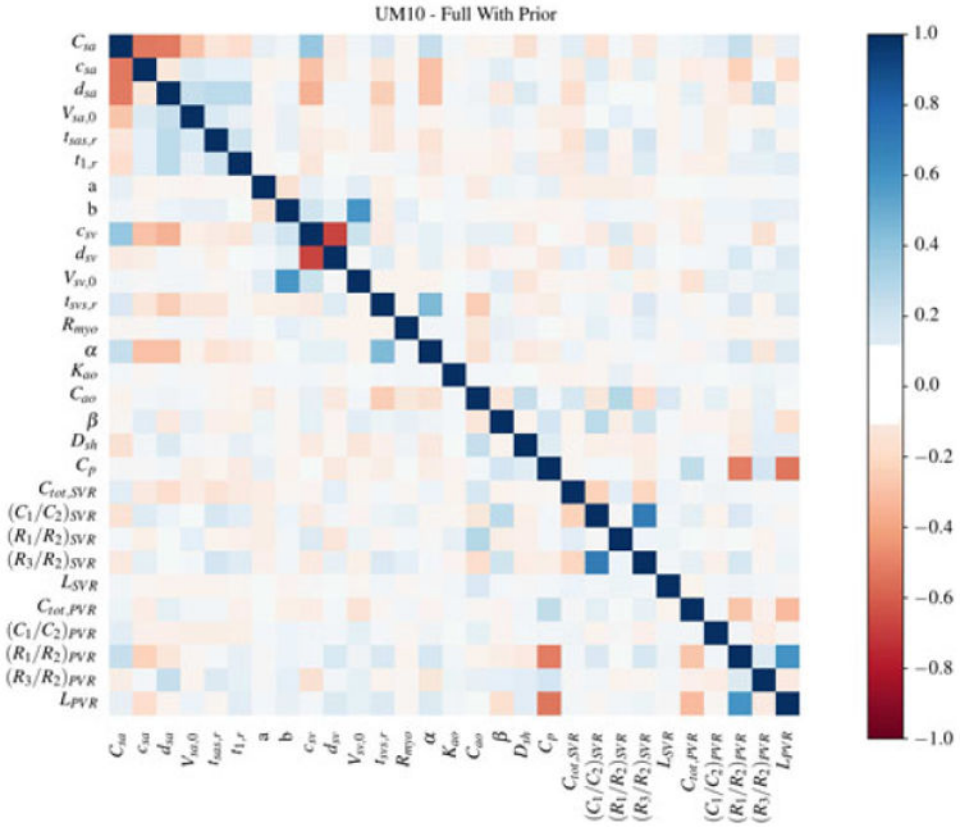

Figure 14.
Parameter correlation matrix computed from MCMC using multi-level Bayesian inference for patient UM10.

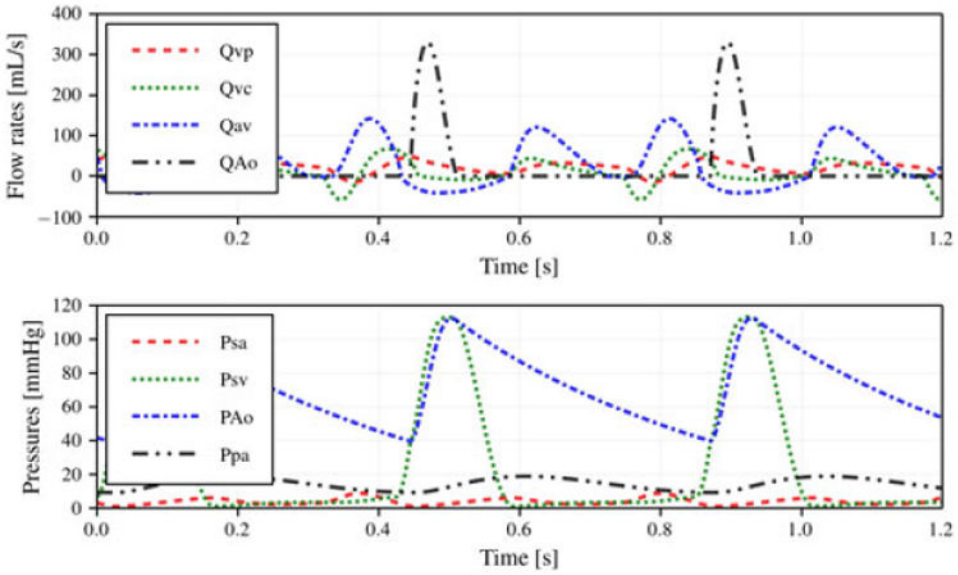

Figure 15.
Flow and pressure time tracings estimated for patient UM10. The regurgitant AV valve flow rate, pulmonary and caval vein flows and pressure tracings are consistent with the expected physiology.

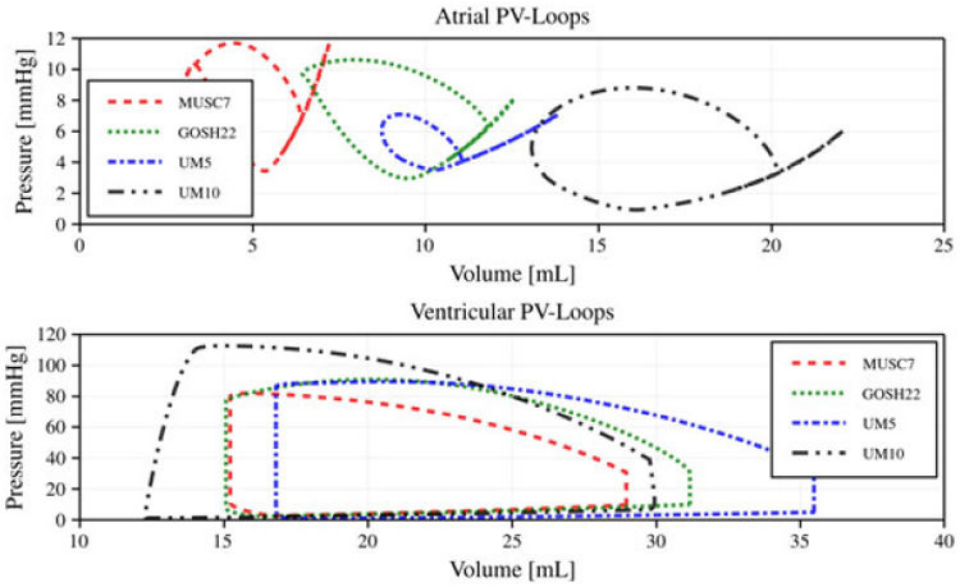

Figure 16.
Atrial and ventricular PV-loops for all patients. Ventricular PV-loops are similar for the four patients, consistently with the similarity in the BSA. Isovolumic contraction and relaxation are not present in patient UM10 due to AV valve regurgitation, as expected. Larger atrial volumes are observed for patient UM10, again consistent with leakage in the AV valve

Table I

List of acronyms.

Acronym	Description	Acronym	Description
MRI	Magnetic resonance imaging	MCMC	Markov chain Monte Carlo
BT	Blalock-Thomas-Taussig	MAP	Maximum a posteriori
SVR	Systemic vascular resistance	DREAM	Differential evolution adaptive Metropolis
PVR	Pulmonary vascular resistance	NM	Nelder-Mead
AV	Atrio-ventricular	GR	Gelman-Rubin
ODE	Ordinary differential equation	SDMA	Maxima and minima in biphasic flow rate
LPN	Lumped parameter network	PV-loop	Pressure-volume loop
FIM	Fisher Information matrix	PA	Pulmonary arteries
SVC	Superior vena cava		
Pedix	Description	Pedix	Description
sa	single atrium	sv	single ventricle
ao	aorta	av	atrio-ventricular
s	systemic	p/lung	pulmonary
ub	upper body	lb	lower body
myo	myocardial	sh	shunt
vc	venae cavae	pv	pulmonary veins
fw	forward	bw	backwords
*a	(suffix) arterial	*v	(suffix) venous

Table II

List of parameters and initial conditions.

	Heart sub-model				Norwood circulation model		
n.	**Parameter**	**Units**	**Description**	**n.**	**Parameter**	**Units**	**Description**
1	HR	[bpm]	Heart rate	1	D_{sh}	[mm]	Shunt diameter
2	C_{sa}	[mmHg]	Passive atrial curve	2	SVR	[mmHg·s cm^{-3}]	Systemic vascular resistance
3	$V_{sa,0}$	[cm^3]	Unstressed atrial volume	3	$C_{tot,SVR}$	[cm^3 mmHg^{-1}]	Total systemic compliance
4	$t_{1,r} = t_1/t_c$	-	AV activation overlap	4	$(C_1/C_2)_{SVR}$	-	Systemic compliance ratio
5	b	[mmHg cm^{-3}]	Active ventricular curve slope	5	$(R_1/R_2)_{SVR}$	-	Systemic resistance ratio 1
6	d_{sv}	[cm^{-3}]	Passive ventricular curve	6	$(R_3/R_2)_{SVR}$	-	Systemic resistance ratio 2
7	$t_{\mathrm{SVS},r} = t_{\mathrm{SVS}}/\sqrt{t_c}$	[s$^{1/2}$]	Ventricular activation time ratio	7	L_{SVR}	[mmHg s^2 cm^{-3}]	Systemic inductance
8	a	-	AV valve resistance coefficient	8	C_p	[cm^3 mmHg^{-1}]	Shunt/PA compliance
9	C_{ao}	[cm^3 mmHg^{-1}]	Aortic compliance	9	PVR	[mmHg s cm^{-3}]	Pulmonary vascular resistance
10	β	-	AV valve inductance coefficient	10	$C_{tot,PVR}$	[cm^3 mmHg^{-1}]	Total pulmonary compliance
11	$1/C_{sa}$	mmHg cm^{-3}	Active atrial curve slope	11	$(C_1/C_2)_{PVR}$	-	Pulmonary compliance ratio
12	d_{sa}	[cm^{-3}]	Increase in the passive atrial curve	12	$(R_1/R_2)_{PVR}$	-	Pulmonary resistance ratio 1
13	$t_{\mathrm{SAS},r} = t_{\mathrm{SAS}}/\sqrt{t_c}$	[s$^{1/2}$]	Atrial activation time ratio	13	$(R_3/R_2)_{PVR}$	-	Pulmonary resistance ratio 2
14	a	[mmHg cm^{-6}]	Curvature on active ventricular curve	14	L_{Pvr}	[mmHg s^2 cm^{-3}]	Pulmonary inductance
15	c_{sv}	[mmHg]	Passive ventricular curve constant				
16	$V_{sv,0}$	[cm^3]	Unstressed ventricular volume				
17	R_{myo}	[mmHg s cm^{-3}]	Myocardial fiber viscous resistance				
18	K_{ao}	[mmHg s^2 cm^{-6}]	Non linear aortic valve resistance				
19	t_d	[s]	Venous and aortic flow rate time delay				
20	k_{bw}	-	AV valve backflow area ratio				

	Heart sub-model				Norwood circulation model		
n.	Initial condition	Units	Description	n.	Initial condition	Units	Description

Heart sub-model				Norwood circulation model			
n.	**Parameter**	**Units**	**Description**	**n.**	**Parameter**	**Units**	**Description**
1	V_{sv}	[cm^3]	Initial ventricular volume	1	P_{ubv}	[mmHg]	Pressure in superior vena cava
2	V_{sa}	[cm^3]	Initial atrial volume	2	P_{uba}	[mmHg]	Arterial pressure in upper body
3	P_{ao}	[mmHg]	Initial aortic pressure	3	P_{pv}	[mmHg]	Pulmonary veins pressure
4	Q_{av}	[cm^3 s^{-1}]	Initial atrioventricular flow	4	P_{pa}	[mmHg]	Pressure in main pulmonary artery
				5	Q_{uba}	[cm^3 s^{-1}]	Flow in the upper body arteries
				6	P_{lung}	[mmHg]	Lung pressure
				7	Q_{pa}	[cm^3 s^{-1}]	Flow in the PA

Table III

Patient data at Norwood surgery.

Patient	**age (months)**	**BSA [m^2]**	**AV Valve area A_{fw} [cm^2]**	**Heart Rate [bpm]**
MUSC7	3	0.26	2.8	117.65
GOSH22	4	0.27	3.3	116.0
UM5	4	0.28	4.2	90.0
UM10	5	0.34	3.7	141.0

Patient	pathology	MR shunt diameter [mm]	SVR [mmHg·s cm^{-3}]	PVR [mmHg·s cm^{-3}]
MUSC7	HRHS, tric., pulm. atresia	4.0	3.07	0.750
GOSH22	HLHS, Ao, mitral atresia	3.5	3.15	0.301
UM5	HLHS, Ao, mitral atresia	4.0	3.17	0.663
UM10	HLHS, Ao, mitral atresia	4.0	6.18	0.500

BSA - Body surface Area; MR - Magnetic resonance; HRHS - Hypoplastic right heart syndrome; HLHS -Hypoplastic left heart syndrome; tric. - tricuspid valve; pulm. - pulmonary

Table IV

Patient-specific target clinical quantities used for parameter identification in both the heart sub-model and full circulation model with systemic and pulmonary circulation blocks.

n.	Target Qty.	Units	Description
1	$P_{ao,av}$	[mmHg]	Average aortic pressure
2	$P_{ao,max}$	[mmHg]	Maximum aortic pressure
3	$P_{sa,av}$	[mmHg]	Average atrial pressure
7	$P_{sa,max}$	[mmHg]	Maximum atrial pressure
4	$P_{sv,max}$	[mmHg]	Maximum ventricular pressure
5	$V_{sv,max}$	[cm^3]	Maximum ventricular volume
6	$P_{sv,0}$	[mmHg]	Ventricular pressure at the start of systole
8	$Q_{reg,av}$	[$cm^3\ s^{-1}$]	Average regurgitant flow rate in AV valve
9	$P_{ao,min}$	[mmHg]	Minimum aortic pressure
11	Q_p/Q_s	-	Pulmonary to systemic flow split ratio
12	$P_{pa,av}$	[mmHg]	Average pulmonary pressure
14	$P_{pa,min}$	[mmHg]	Minimum pulmonary pressure
15	$P_{pa,max}$	[mmHg]	Maximum pulmonary pressure
16	CO	[$cm^3\ s^{-1}$]	Cardiac output
17	$Q_{vc,S}$	[$cm^3\ s^{-1}$]	Flow rate in venae cavae, point S
18	$Q_{vc,M}$	[$cm^3\ s^{-1}$]	Flow rate in venae cavae, point M
19	$Q_{vc,D}$	[$cm^3\ s^{-1}$]	Flow rate in venae cavae, point D
20	$Q_{vc,A}$	[$cm^3\ s^{-1}$]	Flow rate in venae cavae, point A
21	$Q_{pv,S}$	[$cm^3\ s^{-1}$]	Flow rate in pulmonary veins, point S
22	$Q_{pv,M}$	[$cm^3\ s^{-1}$]	Flow rate in pulmonary veins, point M
23	$Q_{pv,D}$	[$cm^3\ s^{-1}$]	Flow rate in pulmonary veins, point D
24	$Q_{pv,A}$	[$cm^3\ s^{-1}$]	Flow rate in pulmonary veins, point A

Table V

Parameter ranges for heart and full circulation models.

Heart model parameters ranges				Full model parameters ranges			
Parameter	**Units**	**Min**	**Max**	**Parameter**	**Units**	**Min**	**Max**
C_{sa}	[cm^3 mmHg^{-1}]	0.05	2.0	D_{sh}	[mm]	2.5	3.5
c_{sa}	[mmHg]	0.01	0.8	C_p	[cm^3 mmHg^{-1}]	0.1	0.4
d_{sa}	[cm^{-3}]	0.16	0.8	τ_{SVR}	[s]	0.5	3.0
$V_{sa,0}$	[cm^3]	00.1	15.0	$(C_1/C_2)_{SVR}$	-	0.1	20.0
$t_{sas,r}$	[s$^{1/2}$]	0.1739	0.2599	$(R_1/R_2)_{SVR}$	-	0.01	3.0
$t_{1,r}$	-	0.01	0.15	$(R_3/R_2)_{SVR}$	-	0.01	3.0
a	[mmHg cm^{-6}]	−0.20	−0.005	L_{SVR}	[mmHg s^2 cm^{-3}]	0.005	0.05
b	[mmHg cm^{-3}]	8.0	15.0	τ_{PVR}	[s]	0.5	3.0
c_{sv}	[mmHg]	0.1	5.0	$(C_1/C_2)_{PVR}$	-	0.1	20.0
d_{sv}	[cm^{-3}]	0.04	0.08	$(R_1/R_2)_{PVR}$	-	0.01	3.0
$V_{sv,0}$	[cm^3]	2.0	15.0	$(R_3/R_2)_{PVR}$	-	0.01	3.0
$t_{svs,r}$	[s$^{1/2}$]	0.2478	0.3718	L_{PVR}	[mmHg s^2 cm^{-3}]	0.005	0.05
R_{myo}	[mmHg s cm^{-3}]	0.001	0.1	V_{sv}	[cm^3]	5.0	40.0
α	-	1.0	30.0	V_{sa}	[cm^3]	1.0	15.0
K_{ao}	[mmHg s^2 cm^{-6}]	1.0E-04	2.5E-4	P_{ao}	[mmHg]	10.0	80.0
C_{ao}	[cm^3 mmHg^{-1}]	0.05	1.0				
β	-	0.0	1.0				
t_d	[s]	−0.2	0.2				
k_{bw}	-	1.0e-5	0.05				

Table VI

Selected scenarios for RCRCR parameter estimation.

Scen.	Parameters	Data
SC1	All parameters and initial conditions	All data
SC2	(5) R_{tot}, τ, C_1/C_2, R_1/R_2, R_3/R_2	(5) $P_{0,min}$, $P_{0,av}$, $P_{0,max}$, $P_{3,av}$, $P_{3,max}$
SC3	(5) R_{tot}, τ, C_1/C_2, R_1/R_2, $R_3/R2$	(3) $P_{0,av}$, $P_{0,max}$, $P_{3,av}$
SC4	(3) R_{tot}, τ, C_1/C_2	(5) $P_{0,min}$, $P_{0,av}$, $P_{0,max}$, $P_{3,av}$, $P_{3,max}$

Table VII

Estimation of 95% confidence intervals for RCRCR parameters and learning factors θ for scenarios 2, 3, and 4.

Parameter	**Units**	**True average**	**True Std.**	**Adm. range**
R_{tot}	[mmHg s cm^{-3}]	3.07	0.153	[2.0 – 4.0]
τ	[s]	0.56	0.028	[0.5 – 3.0]
C_1/C_2	-	0.2	0.01	[0.1 – 10.0]
R_1/R_2	-	0.2	0.01	[0.1 – 2.0]
R_3/R_2	-	0.2	0.01	[0.1 – 1.0]
$P_{1,i}$	[mmHg]	5	0.25	-
$P_{2,i}$	[mmHg]	5	0.25	-
Parameter	Units	Scenario 2	Scenario 3	Scenario 4
R_{tot}	[mmHg s cm^{-3}]	[2.931 – 3.967]	[3.161 – 4.069]	[2.943 – 3.189]
τ	[s]	[0.494 – 0.564]	[0.347 – 2.705]	[0.522 – 0.600]
C_1/C_2	-	[0.164 – 0.750]	[0.062 – 0.838]	[0.173 – 0.229]
R_1/R_2	-	[0.201 – 0.777]	[0.425 – 1.021]	[0.2 – 0.2]
R_3/R_2	-	[0.108 – 0.604]	[0.052 – 0.684]	[0.2 – 0.2]
$P_{1,i}$	[mmHg]	[5 – 5]	[5 – 5]	[5 – 5]
$P_{2,i}$	[mmHg]	[5 – 5]	[5 – 5]	[5 — 5]
Learning factor θ	Units	Scenario 2	Scenario 3	Scenario 4
R_{tot}	[mmHg s cm^{-3}]	0.455	0.522	0.870
τ	[s]	0.970	0.006	0.967
C_1/C_2	-	0.938	0.917	0.994

Table VIII

Selected virtual patient parameters for the Norwood circulation model.

HR	[bpm]	117.65	d_{SV}	[cm^{-3}]	0.065	SVR	[mmHg s cm^{-3}]	3.07
C_{sa}	[cm^3 mmHg^{-1}]	0.76569	$V_{sv,0}$	[cm^3]	9.7786	PVR	[mmHg s cm^{-3}]	0.75
c_{sa}	[mmHg]	0.01	$t_{svs,r}$	[s$^{1/2}$]	0.31	$C_{tot,SVR}$	[cm^3 mmHg $^{-1}$]	0.76713
d_{sa}	[cm^{-3}]	0.8	R_{myo}	[mmHg s cm^{-3}]	0.1	$(C_1/C_2)_{svr}$	-	5.0
$V_{sa,0}$	[cm^3]	2.5	α	-	24.474	$(R_1/R_2)_{SVR}$	-	0.9
$t_{sas,r}$	[s$^{1/2}$]	0.25	K_{ao}	[mmHg s^2 cm^{-6}]	0.00025	$(R_3/R_2)_{SVR}$	-	0.1
$t_{1,r}$	-	0.1	C_{ao}	[cm^3 mmHg^{-1}]	0.24	L_{SVR}	[mmHg s^2 cm^{-3}]	0.0069709
a	[mmHg cm^{-6}]	−0.12	β	-	0.95	$C_{tot,PVR}$	[cm^3 mmHg^{-1}]	0.97019
b	[mmHg cm^{-3}]	14.0	D_{sh}	[mm]	3.0451	$(C_1/C_2)_{PVR}$	-	5.0
c_{sv}	[mmHg]	1.0	C_p	[cm^3 mmHg^{-1}]	0.31362	$(R_1/R_2)_{PVR}$	-	0.1
P_{lung}	[mmHg]	16.0	P_{pv}	[mmHg]	13.0	Q_{pa}	[cm^3 s^{-1}]	15.0
$(R_3/R_2)_{PVR}$	-	1.0	L_{PVR}	[mmHg s^{-2} cm^{-3}]	0.025568	k_{bw}	-	0.0
V_{sa}	[cm^3]	2.5537	P_{ao}	[mmHg]	38.0	Q_{av}	[cm^3 s^{-1}]	50.0
Q_{uba}	[cm^3 s^{-1}]	14.0	P_{uba}	[mmHg]	15.0	P_{pa}	[mmHg]	10.0
V_{sv}	[cm^3]	38.869	P_{ubv}	[mmHg]	22.0			

Table IX

Target matching under virtual patient identification.

Target quantity	Units	Model results	Target AV	Target SD	Weight
$P_{ao,av}$	[mmHg]	49.6	48.9	2.4	1/2
$P_{ao,min}$	[mmHg]	30.6	31.4	1.6	1
$P_{ao,max}$	[mmHg]	72.6	73.6	3.7	1
$P_{sa,av}$	[mmHg]	6.5	6.5	0.3	1
$P_{sv,max}$	[mmHg]	73.0	74.9	3.7	1
$V_{sv,max}$	[cm^3]	28.3	28.2	1.4	1
Q_p/Q_s	-	0.811	0.8	0.04	1
$P_{pa,av}$	[mmHg]	15.0	15.1	0.76	1
CO	[$cm^3\ s^{-1}$]	25.5	25.3	1.3	1/2
$Q_{vc,S}$	[$cm^3\ s^{-1}$]	25.1	24.7	1.2	8
$Q_{vc,M}$	[$cm^3\ s^{-1}$]	4.9	4.9	0.2	8
$Q_{vc,D}$	[$cm^3\ s^{-1}$]	23.8	24.5	1.2	8
$Q_{vc,A}$	[$cm^3\ s^{-1}$]	5.4	5.4	0.3	8
$Q_{pv,S}$	[$cm^3\ s^{-1}$]	21.2	19.6	1.0	12
$Q_{pv,M}$	[$cm^3\ s^{-1}$]	0.24	0.24	0.01	12
$Q_{pv,D}$	[$cm^3\ s^{-1}$]	16.6	16.1	0.8	12
$Q_{pv,A}$	[$cm^3\ s^{-1}$]	7.2	7.1	0.4	12
$P_{pa,min}$	[mmHg]	13.4	13.4	0.7	1
$P_{pa,max}$	[mmHg]	17.3	17.2	0.9	1
$P_{sv,0}$	[mmHg]	2.3	2.3	0.8	1
$P_{sa,max}$	[mmHg]	12.4	12.2	0.6	1

Table X

Virtual patient parameters and computed MAP estimates for Norwood circulation model. Rows in gray indicate close agreement between true and estimated parameters.

Parameter	Units	Virtual patient	MAP estimate*	Norm. dist. [%]
HR	[bpm]	117.65	117.65	-
C_{sa}	[cm^3 $mmHg^{-1}$]	0.766	0.472	15.0
c_{sa}	[mmHg]	0.01	0.29	35.2
d_{sa}	[cm^{-3}]	0.8	0.55	38.9
$V_{sa,0}$	[cm^3]	2.5	0.28	14.9
$t_{sas,r}$	-	0.25	0.19	65.5
$t_{1,r}$	-	0.1	0.03	52.3
a	[mmHg cm^6]	−0.12	−0.17	24.3
b	[mmHg cm^{-3}]	14.0	11.9	30.6
c_{sv}	[mmHg]	1.0	2.2	23.6
d_{sv}	[cm^{-3}]	0.065	0.036	71.7
$V_{sv,0}$	[cm^3]	9.8	8.4	10.3
$t_{svs,r}$	-	0.31	0.35	31.5
R_{myo}	[mmHg s cm^{-3}]	0.1	0.12	16.9
α	-	24.5	16.2	28.5
K_{ao}	[mmHg s^2 cm^{-6}]	0.000250	0.000173	51.3
C_{ao}	[cm^3 $mmHg^{-1}$]	0.24	0.24	0.35
β	-	0.95	0.12	82.8
D_{sh}	[mm]	3.0	3.0	2.7
C_p	[cm^3 $mmHg^{-1}$]	0.31	0.17	47.8
SVR	[mmHg s cm^{-3}]	3.07	3.07	-
PVR	[mmHg s cm^{-3}]	0.75	0.75	-
$C_{tot,SVR}$	[cm^3 $mmHg^{-1}$]	0.77	0.52	30.3
$(C_1/C_2)_{SVR}$	-	5.0	5.8	4.2
$(R_1/R_2)_{SVR}$	-	0.9	3.7	93.1
$(R_3/R_2)_{SVR}$	-	0.1	0.04	2.2
L_{SVR}	[mmHg s^2 cm^{-3}]	0.007	0.021	32.1
$C_{tot,PVR}$	[cm^3 $mmHg^{-1}$]	0.97	1.20	7.0
$(C_1/C_2)_{PVR}$	-	5.0	4.8	1.0
$(R_1/R_2)_{PVR}$	-	0.1	0.3	7.7

Parameter	Units	Virtual patient	MAP estimate*	Norm. dist. [%]
$(R_3/R_2)_{PVR}$	-	1.0	1.3	9.4
L_{PVR}	[mmHg s^2 cm^{-3}]	0.026	0.032	14.6
k_{bw}	-	0.0	0.0	-
V_{sv}	[cm^3]	38.9	26.1	36.4
V_{sa}	[cm^3]	2.6	1.3	9.3
P_{ao}	[mmHg]	38.0	36.8	1.7
Q_{av}	[cm^3 s^{-1}]	50.0	50.0	-
P_{ubv}	[mmHg]	22.0	22.0	-
Q_{uba}	[cm^3 s^{-1}]	14.0	14.0	-
P_{uba}	[mmHg]	15.0	15.0	-
P_{lung}	[mmHg]	16.0	16.0	-
P_{pv}	[mmHg]	13.0	13.0	-
Q_{pa}	[cm^3 s^{-1}]	15.0	15.0	-
P_{pa}	[mmHg]	10.0	10.0	-

* ℓ^2 distance between true parameters and MAP estimate is equal to 0.316.

Table XI

Parameter learning factors θ for Bayesian estimation of heart and full circulation models.

Patient	Heart average θ	Single-level average θ	Multi-level average θ
MUSC7	0.30	0.28	0.41
GOSH22	0.30	0.31	0.41
UM5	0.21	0.28	0.38
UM10	0.26	0.26	0.35

Patient	Multi-level improvement Average θ_M/θ_S^*	$V_{sa,0}$ $\theta_S - \theta_M$	$t_{1,r}$ θ_M/θ_S
MUSC7	5.62	0.04 - 0.77	0.00 - 0.19
GOSH22	2.64	0.00 - 0.63	0.16 - 0.24
UM5	2.58	0.04 - 0.84	0.03 - 0.33
UM10	3.86	0.00 - 0.66	0.06 - 0.23

*Average learning factor computed from the parameters C_{sa}, c_{sa}, d_{sa}, a, b, c_{sv}, d_{sv}, $V_{sv,0}$, $t_{svs,r}$, R_{myo}, C_{ao}, θ_M is parameter learning factor under multi-level estimation, while θ_S is the same quantity for single-level estimation.

Table XII

Target table for patients MUSC7 and GOSH22.

		MUSC7			GOSH22			
Target quantity	**Units**	**Model results**	**Target AV**	**Target SD**	**Model results**	**Target AV**	**Target SD**	**Weight**
$P_{Ao,av}$	[mmHg]	52.8	53.0	2.7	51.0	51.0	2.6	1/2
$P_{Ao,min}$	[mmHg]	30.7	30.0	1.5	30.9	31.0	1.6	1
$P_{Ao,max}$	[mmHg]	81.4	80.0	4.0	78.1	78.0	3.9	1
$P_{sa,av}$	[mmHg]	7.2	7.0	0.4	6.1	6.0	0.3	1
$P_{sv,max}$	[mmHg]	81.9	82.0	4.1	90.9	91.0	4.6	1
$V_{sv,max}$	[cm^3]	29.0	29.0	1.45	31.2	31.0	1.6	1
Q_p/Q_s	-	0.8	0.8	0.04	1.2	1.2	0.06	1
$P_{pa,av}$	[mmHg]	16.2	16.0	0.8	11.2	11.0	0.6	1
CO	[$cm^3\ s^{-1}$]	27.0	27.0	1.4	31.1	30.9	1.5	1/2
$Q_{vc,S}$	[$cm^3\ s^{-1}$]	38.9	43.0	2.6	40.2	42.0	2.1	8
$Q_{vc,M}$	[$cm^3\ s^{-1}$]	3.3	−1.5	−0.08	1.3	1.3	0.07	8
$Q_{vc,D}$	[$cm^3\ s^{-1}$]	38.5	36.0	1.8	26.3	23.0	1.2	8
$Q_{vc,A}$	[$cm^3\ s^{-1}$]	−9.8	−16.5	−0.8	−9.2	−5.2	−0.3	8
$Q_{pv,S}$	[$cm^3\ s^{-1}$]	14.1	13.0	0.7	24.3	28.0	1.4	12
$Q_{pv,M}$	[$cm^3\ s^{-1}$]	4.2	4.0	0.2	11.6	10.5	0.5	12
$Q_{pv,D}$	[$cm^3\ s^{-1}$]	18.0	23.0	1.2	29.7	30.0	1.5	12
$Q_{pv,A}$	[$cm^3\ s^{-1}$]	7.4	7.5	0.4	5.5	6.7	0.3	12
$P_{pa,min}$	[mmHg]	10.5	10.8	0.5	7.5	-	-	1
$P_{pa,max}$	[mmHg]	23.0	24.2	1.2	15.7	-	-	1
$Q_{reg,av}$	[$cm^3\ s^{-1}$]	-	-	-	-	-	-	1
$P_{sv,0}$	[mmHg]	9.4	9.9	0.8	9.8	10.0	0.5	1
$P_{sa,max}$	[mmHg]	11.7	11.4	0.6	10.6	11.0	0.6	1

Table XIII

Target table for patients UM5 and UM10.

		UM5			UM10			
Target quantity	**Units**	**Model results**	**Target AV**	**Target SD**	**Model results**	**Target AV**	**Target SD**	**Weight**
$P_{ao,av}$	[mmHg]	53.4	53.0	2.7	72.2	72.0	3.6	1/2
$P_{ao,min}$	[mmHg]	30.3	30.0	1.5	39.7	40.0	2.0	1
$P_{ao,max}$	[mmHg]	87.5	87.0	4.3	112.3	113.0	5.7	1
$P_{sa,av}$	[mmHg]	5.0	5.0	0.3	4.0	4.0	0.2	1
$P_{sv,max}$	[mmHg]	89.4	90.0	4.5	113.0	114.0	5.7	1
$v_{sv,max}$	[cm^3]	35.5	35.5	1.8	30.0	30.0	1.5	1
Q_p/Q_s	-	0.8	0.8	0.04	1.8	1.8	0.09	1
$P_{pa,av}$	[mmHg]	13.4	13.4	0.7	14.0	14.0	0.7	1
CO	[$cm^3\ s^{-1}$]	28.0	27.0	1.4	31.2	31.0	1.6	1/2
$Q_{vc,S}$	[$cm^3\ s^{-1}$]	25.3	24.5	1.2	66.8	67.0	3.4	8
$Q_{vc,M}$	[$cm^3\ s^{-1}$]	−0.8	−1.9	−0.09	-	-	-	8
$Q_{vc,D}$	[$cm^3\ s^{-1}$]	28.6	42.8	2.1	-	-	-	8
$Q_{vc,A}$	[$cm^3\ s^{-1}$]	9.0	14.9	0.7	−57.6	−83.0	−4.2	8
$Q_{pv,S}$	[$cm^3\ s^{-1}$]	15.5	13.9	0.7	47.3	47.3	2.4	12
$Q_{pv,M}$	[$cm^3\ s^{-1}$]	8.0	7.7	0.4	-	-	-	12
$Q_{pv,D}$	[$cm^3\ s^{-1}$]	15.9	22.6	1.1	-	-	-	12
$Q_{pv,A}$	[$cm^3\ s^{-1}$]	7.0	11.8	0.6	−14.8	−29.0	−1.5	12
$P_{pa,min}$	[mmHg]	11.8	12.4	0.6	9.2	9.2	0.5	1
$P_{pa,max}$	[mmHg]	17.7	18.3	0.9	18.8	18.8	0.9	1
$Q_{reg,av}$	[$cm^3\ s^{-1}$]	-	-	-	10.5	10.5	0.5	1
$P_{sv,0}$	[mmHg]	4.9	6.3	1.6	6.7	6.6	1.7	1
$P_{sa,max}$	[mmHg]	7.1	7.0	0.2	8.8	8.8	0.6	1